

---

# BAYPRANOMETA: BAYESIAN PROTO-MAML FOR FEW-SHOT INDUSTRIAL IMAGE ANOMALY DETECTION

---

**Soham Sarkar**

Indian Institute of Technology Kanpur  
Kanpur, India

**Tanmay Sen**

Indian Statistical Institute Kolkata  
Kolkata, India

**Sayantan Banerjee** \*

Indian Institute of Management Indore  
Indore, India

## ABSTRACT

Industrial image anomaly detection is a challenging problem owing to extreme class imbalance and the scarcity of labeled defective samples, particularly in few-shot settings. We propose BayPrAnoMeta, a Bayesian generalization of Proto-MAML for few-shot industrial image anomaly detection. Unlike existing Proto-MAML approaches that rely on deterministic class prototypes and distance-based adaptation, BayPrAnoMeta replaces prototypes with task-specific probabilistic normality models and performs inner-loop adaptation via a Bayesian posterior predictive likelihood. We model normal support embeddings with a Normal–Inverse–Wishart (NIW) prior, producing a Student- $t$  predictive distribution that enables uncertainty-aware, heavy-tailed anomaly scoring and is essential for robustness in extreme few-shot settings. We further extend BayPrAnoMeta to a federated meta-learning framework with supervised contrastive regularization for heterogeneous industrial clients and prove convergence to stationary points of the resulting nonconvex objective. Experiments on the MVTec AD benchmark demonstrate consistent and significant AUROC improvements over MAML, Proto-MAML, and PatchCore-based methods in few-shot anomaly detection settings.

**Keywords:** Bayesian modeling, Model-Agnostic Meta-Learning, Federated learning, Contrastive learning, Anomaly detection.

## 1 Introduction

Modern manufacturing requires automated anomaly detection even for minor defects, such as scratches, deformations, and contamination, which can significantly hamper product quality and result in expensive operational failures (Bergmann et al., 2019; Ruff et al., 2018). Despite its importance, anomaly detection in an industrial setting is difficult for several reasons. First, the nature of anomalies (rare and visually diverse) within datasets dominated by normal samples makes large-scale supervised training unfeasible (Pang et al., 2021). Moreover, significant domain shifts, which originate from different machines, sensors, and production sites, obstruct the generalization of models (Li et al., 2025). Privacy and data-sharing limitations are frequently a result of legal and intellectual property issues, which, in turn, hinder the aggregation of visual inspection data across different manufacturing facilities (Kairouz et al., 2021). Together, these factors demonstrate why classical supervised learning approaches are inadequate and motivate the development of few-shot, uncertainty-aware anomaly detection methods.

A prominent line of work in industrial anomaly detection focuses on nearest-neighbor and representation-based methods that model normality using only defect-free samples. Approaches such as PatchCore (Roth et al., 2022) and Reverse Distillation (Tien et al., 2023) achieve strong performance in fully unsupervised settings by leveraging powerful pretrained feature extractors. However, such methods rely on fixed representations and distance-based inference, which limits their ability to adapt to new object categories, configurations, or operating conditions when only a small number of

---

\*Corresponding author, email: sayantanb@iimindr.ac.in

labeled samples are available. In practical industrial environments, limited labeled anomalies or configuration-specific feedback are often available, motivating methods that can explicitly adapt to new tasks from few examples. Meta-learning provides a natural framework for this setting by enabling rapid task-specific adaptation (Hospedales et al., 2021). In particular, episodic meta-learning methods such as Prototypical Networks (Snell et al., 2017) and Model-Agnostic Meta-Learning (MAML) (Finn et al., 2017) align well with industrial scenarios where only a few labeled samples are available per object type or configuration. Nevertheless, standard meta-learning approaches are primarily discriminative and do not provide calibrated uncertainty estimates, which are crucial for reliable decision-making in anomaly detection under extreme data scarcity (Malinin and Gales, 2018).

To address these challenges more rigorously, we introduce a novel unified framework that integrates few-shot adaptation, uncertainty-aware modeling, and privacy-constrained deployment. In this framework, we propose *(i)* BayPrAnoMeta, a Bayesian Proto-MAML method, where we place a Normal-Inverse-Wishart (NIW) prior on the class support embeddings, yielding a multivariate Student- $t$  posterior predictive distribution (Murphy, 2012) to support robust heavy-tailed modeling suitable for anomalies (Gordon et al., 2018) and likelihood-based anomaly scoring; *(ii)* a federated learning (McMahan et al., 2017; Chen et al., 2018) formulation to account for client heterogeneity and non i.i.d. data distributions, enabling scalable and privacy-preserving deployment across distributed industrial environments; *(iii)* a supervised contrastive loss (Khosla et al., 2020) within this federated framework to enhance representation quality under client heterogeneity.

## 2 Related Work

Early research on industrial anomaly detection focuses on unsupervised learning or one-class learning approaches where standard datasets such as MVTec AD (Bergmann et al., 2019) have been used for empirical evaluation. Furthermore, Deep One-Class Classification (Ruff et al., 2018) and subsequent surveys (Pang et al., 2021) focus on core challenges such as class imbalance, heterogeneous defect patterns, and limited labeled anomaly samples. Due to their reliance on large training datasets and their difficulty handling unseen anomaly types, classical anomaly detection methods have limited applicability.

Meta-learning provides a general framework for rapid adaptation under limited supervision. Metric-based approaches such as Prototypical Networks (Snell et al., 2017), Matching Networks (Vinyals et al., 2016), Relation Networks (Sung et al., 2018) learn embedding spaces where few-shot classification can be performed via distance-based inference whereas gradient based methods such as MAML (Finn et al., 2017) and its variants (Reptile, MetaSGD) enable fast adaptation through parameter initialization optimized across tasks. (Hospedales et al., 2021) summarize these developments and their applicability across several domains. Meta-learning provides a promising alternative to conventional supervised learning when the number of clean samples is limited. However, most of the approaches heavily rely on discriminative objectives and standard techniques provide point estimates rather than uncertainty-aware predictions, which limits their application in the industrial systems.

In anomaly detection, uncertainty estimation plays a critical role, where models must be able to detect deviations rather than only classifying known categories. Several probabilistic approaches such as Prior Networks (Malinin and Gales, 2018) and Bayesian neural networks provide mechanisms for capturing this uncertainty. Representative methods include probabilistic MAML, hierarchical Bayesian meta-learning (Grant et al., 2018), and variational inference based meta learners. Gordon et al. (2018) show that probabilistic inference can be integrated into meta-learning, facilitating closed-form posterior updates. Classical Bayesian models support robust modeling under few-shot settings. Specifically, placing a Normal-Inverse-Wishart (NIW) prior on class-conditional embeddings with a multivariate Student- $t$  posterior distribution offers heavy-tailed robustness desirable for anomaly detection (Murphy, 2012) which we adopt as the foundation in our paper.

Contrastive learning has been increasingly adopted in anomaly detection to improve the structure of learned feature representations by using label information to shape embedding geometry more explicitly (Khosla et al., 2020). In the context of industrial anomaly detection, several methods exploit contrastive principles to encourage separation between normal and defective samples. For instance, recent methods such as PaDiM (Defard et al., 2021), and OCR-GAN (Liang et al., 2023) utilize a contrastive approach to shaping features, though they lack explicit supervision across several types of anomalies. However, these approaches typically operate in centralized settings and do not explicitly address non-i.i.d. data distributions or client-level heterogeneity.

Recent studies like FedAvg by McMahan et al. (2017) and comprehensive reviews like Kairouz et al. (2021) highlight the main considerations in Federated Learning (FL) design (e.g., communication efficiency, client heterogeneity, and statistical bias, among others). Federated meta-learning integrates FL with rapid task adaptation. While early work by Chen et al. (2018) focuses meta-learning formulations in decentralized settings, Fallah et al. (2020) explores personalized

federated learning methods inspired by MAML, including Per-FedAvg, which allows client-level personalization through local adaptation.

Existing anomaly detection methods excel in isolated settings but rarely address few-shot adaptation, uncertainty estimation, task-specific representation learning, and privacy constraints simultaneously. To address these challenges in a unified manner, we integrate Bayesian Proto-MAML, supervised contrastive learning, and federated meta-learning into a single framework tailored to real-world industrial anomaly detection. Figure 1 illustrates the resulting architecture, comprising a shared embedding network, task-specific Bayesian normality models in the embedding space, and a federated meta-learning loop across heterogeneous clients.

The rest of the paper is organized as follows. We present our methodology and algorithm in Section 3, with theoretical guarantees in Section 4. Experimental results and discussion are presented in Section 5, with conclusion in Section 6. Details of experiments and algorithms, proofs of results, error analysis, and additional experimental results are included in the Appendix. Code and results for BayPrAnoMeta and all other methods are available at <https://anonymous.4open.science/r/BayPrAnoMeta-77A1>.

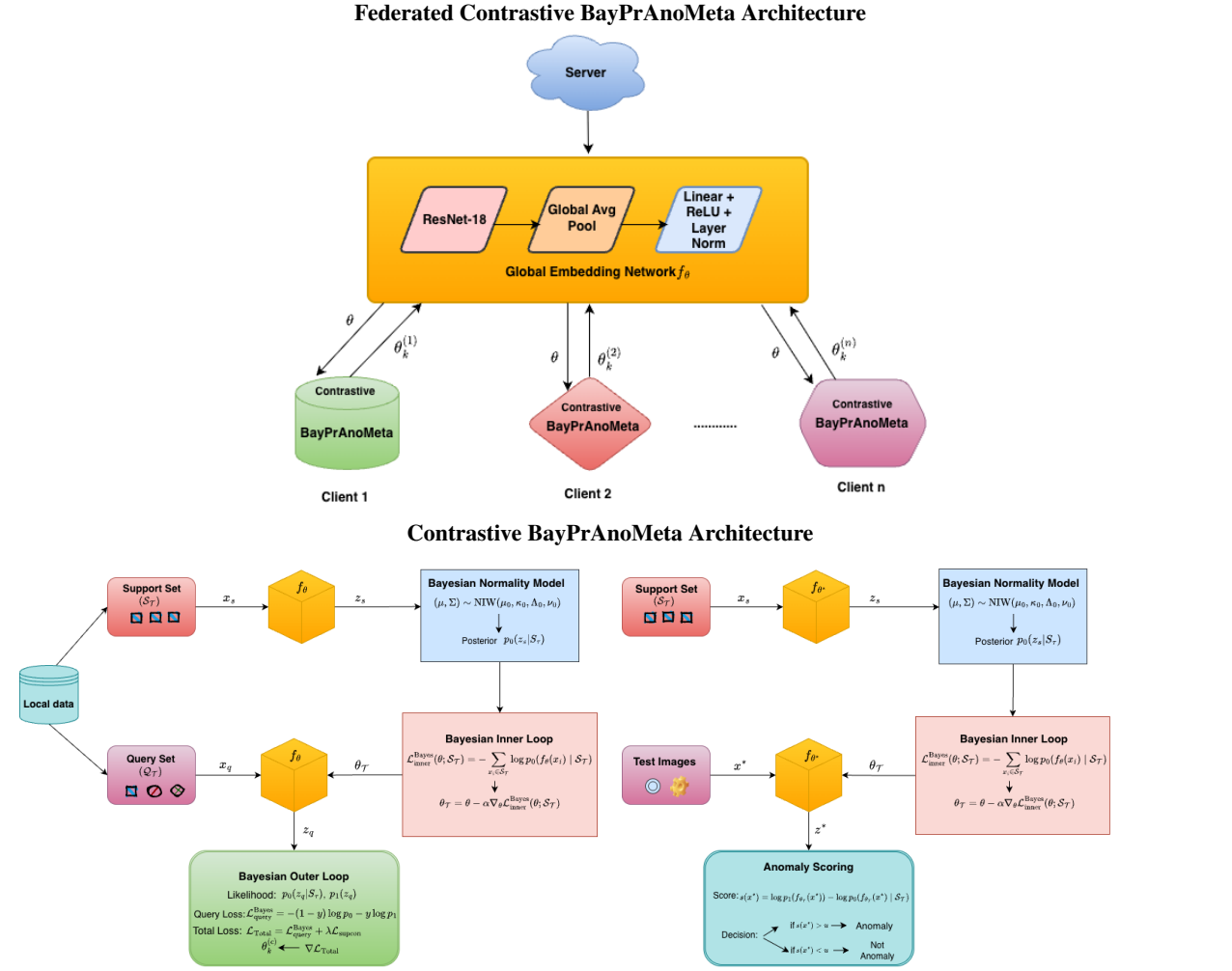


Figure 1: Top: Federated Contrastive BayPrAnoMeta framework, where locally each client uses Contrastive BayPrAnoMeta for industrial image anomaly detection. Bottom: (a) training framework of Contrastive BayPrAnoMeta of a particular client  $c$  which uses the global embedding network  $f_\theta$  and after the  $k^{\text{th}}$  round of training sends the updated parameter  $\theta_k^{(c)}$  to the global server, and (b) testing framework of Contrastive BayPrAnoMeta of that client  $c$ , which takes the globally trained parameter  $\theta^*$  as input for adaptation during inference for anomaly detection.

### 3 Methodology

#### 3.1 BayPrAnoMeta: Proposed Bayesian Proto-MAML for few-shot anomaly detection

**Problem formulation** Let  $\mathcal{X}$  denote the space of input images and let  $f_\theta : \mathcal{X} \rightarrow \mathbb{R}^d$  be a neural embedding function parameterized by  $\theta$ . The data is assumed to be drawn from multiple industrial object categories, each of which is modeled as a task  $\mathcal{T} \sim p(\mathcal{T})$ . For each task  $\mathcal{T}$ , learning proceeds episodically via an episode  $\mathcal{E}_\mathcal{T} = (\mathcal{S}_\mathcal{T}, \mathcal{Q}_\mathcal{T})$ , where the support set  $\mathcal{S}_\mathcal{T} = \{x_i\}_{i=1}^K$  consists exclusively of normal samples, and the query set  $\mathcal{Q}_\mathcal{T} = \{(x_j, y_j)\}$  contains both normal and anomalous samples, with labels  $y_j \in \{0, 1\}$ . Each input image  $x \in \mathcal{X}$  is mapped to a latent representation  $z = f_\theta(x)$ .

**Bayesian modeling of normal embeddings** For a task  $\mathcal{T}$ , we assume embeddings of normal samples follow a Gaussian distribution  $z \mid (\mu, \Sigma) \sim \mathcal{N}(\mu, \Sigma)$ , with a conjugate Normal-Inverse-Wishart (NIW) prior  $(\mu, \Sigma) \sim \text{NIW}(\mu_0, \kappa_0, \Lambda_0, \nu_0)$ . Given support embeddings  $z_i = f_\theta(x_i)$ , denoting  $\bar{z} = \sum_{i=1}^K z_i / K$ ,  $S_z = \sum_{i=1}^K (z_i - \bar{z})(z_i - \bar{z})^\top$ , we get a NIW posterior with parameters

$$\begin{aligned} \kappa_n &= \kappa_0 + K, \quad \nu_n = \nu_0 + K, \quad \mu_n = \frac{\kappa_0 \mu_0 + K \bar{z}}{\kappa_n}, \\ \Lambda_n &= \Lambda_0 + S_z + \frac{\kappa_0 K}{\kappa_n} (\bar{z} - \mu_0)(\bar{z} - \mu_0)^\top. \end{aligned} \quad (1)$$

Marginalizing  $\mu$  and  $\Sigma$  yields the posterior predictive distribution

$$p_0(z \mid \mathcal{S}_\mathcal{T}) = \text{Student-}t(z \mid \mu_n, a_n \Lambda_n, \nu_n - d + 1), \quad (2)$$

where  $a_n = (\kappa_n + 1) / \{\kappa_n(\nu_n - d + 1)\}$ . We denote the predictive scale matrix by  $\Sigma_n := a_n \Lambda_n$ .

**Bayesian inner-loop adaptation** Task-specific adaptation is performed by maximizing the Bayesian likelihood of support samples,

$$\mathcal{L}_{\text{inner}}^{\text{Bayes}}(\theta; \mathcal{S}_\mathcal{T}) = - \sum_{x_i \in \mathcal{S}_\mathcal{T}} \log p_0(f_\theta(x_i) \mid \mathcal{S}_\mathcal{T}), \quad (3)$$

yielding adapted parameters  $\theta_\mathcal{T} = \theta - \alpha \nabla_\theta \mathcal{L}_{\text{inner}}^{\text{Bayes}}(\theta; \mathcal{S}_\mathcal{T})$ .

**Anomaly reference model** To model anomalous embeddings, we introduce a task-independent background distribution

$$p_1(z) = \text{Student-}t(z \mid 0, \sigma^2 I, \nu_a), \quad (4)$$

which assigns non-negligible likelihood to out-of-distribution embeddings and remains fixed across tasks. This anomaly model is used only at test time for likelihood-based anomaly scoring.

**Outer-loop Bayesian meta-objective** Given the task-adapted parameters  $\theta_\mathcal{T}$ , query samples are embedded as  $z_j = f_{\theta_\mathcal{T}}(x_j)$ . For each query pair  $(x_j, y_j) \in \mathcal{Q}_\mathcal{T}$ , the supervised Bayesian query loss is defined as

$$\mathcal{L}_{\text{query}}^{\text{Bayes}} = -[(1 - y_j) \log p_0(z_j \mid \mathcal{S}_\mathcal{T}) + y_j \log p_1(z_j)]. \quad (5)$$

The meta-learning objective minimizes the expected query loss across tasks,

$$\min_{\theta} \mathbb{E}_{\mathcal{T} \sim p(\mathcal{T})} \left[ \sum_{(x_j, y_j) \in \mathcal{Q}_\mathcal{T}} \mathcal{L}_{\text{query}}^{\text{Bayes}}(\theta_\mathcal{T}) \right],$$

with gradients propagated through the Bayesian inner-loop updates, and the meta-parameters optimized via gradient descent with meta-learning rate  $\beta$ :

$$\theta \leftarrow \theta - \beta \nabla_\theta \mathbb{E}_{\mathcal{T} \sim p(\mathcal{T})} \left[ \sum_{(x_j, y_j) \in \mathcal{Q}_\mathcal{T}} \mathcal{L}_{\text{query}}^{\text{Bayes}}(\theta_\mathcal{T}) \right].$$

**Testing and anomaly scoring** At test time, a previously unseen task  $\mathcal{T}$  is provided with a small support set  $\mathcal{S}_{\mathcal{T}}$  containing only normal samples. The posterior predictive distribution  $p_0(\cdot | \mathcal{S}_{\mathcal{T}})$  is computed using the closed-form NIW updates, and the embedding network is adapted via the Bayesian inner loop to obtain  $\theta_{\mathcal{T}}$ . For a test sample  $x^*$ , the anomaly score is defined using a likelihood-ratio criterion,

$$s(x^*) = \log p_1(f_{\theta_{\mathcal{T}}}(x^*)) - \log p_0(f_{\theta_{\mathcal{T}}}(x^*) | \mathcal{S}_{\mathcal{T}}).$$

Samples with larger scores are considered more likely to be anomalous. This likelihood-based scoring provides calibrated, uncertainty-aware anomaly detection without requiring distance normalization. We emphasize that  $\theta$  parameterizes the deterministic embedding network, while we introduce task-specific latent parameters  $(\mu, \Sigma)$  as inferred in closed form from support embeddings.

A key difficulty in few-shot anomaly detection is that  $K$  can be much smaller than the embedding dimension  $d$ . In such regimes, likelihood-based objectives that rely on *empirical* covariance estimates may become ill-posed (e.g. singular covariance when  $K < d$ ), leading to undefined log-likelihoods and unstable gradients. We show that the NIW prior used in BayPrAnoMeta guarantees that the Bayesian predictive model remains well-defined and numerically stable for *any* support size  $K \geq 1$ , including  $K < d$ .

**Proposition 1** (Few-shot well-posedness of the NIW–Student- $t$  predictive). *Assume  $\Lambda_0 \succ 0$  and  $\nu_0 > d - 1$ . Then for every  $K \geq 1$ , every support set  $\mathcal{S}$  of size  $K$ , and every parameter  $\theta$ , the posterior predictive density  $p_0(\cdot | \mathcal{S})$  is a proper multivariate Student- $t$  distribution with (i) strictly positive definite scale matrix  $\Sigma_n \succ 0$ , and (ii) finite log-density  $\log p_0(z | \mathcal{S})$  for all  $z \in \mathbb{R}^d$ . In particular, the predictive model remains well-defined even when  $K < d$ .*

### 3.2 Federated Bayesian Proto-MAML for few-shot anomaly detection with supervised contrastive loss

In reality, data are generated across multiple clients such as machines, production lines, or factories, operating under heterogeneous conditions. These clients cannot share data due to privacy policies and communication constraints, which motivates the federated learning paradigm, where model training is collaborative while data remain local. While Section 3.1 introduces BayPrAnoMeta, a Bayesian Proto-MAML framework for few-shot anomaly detection in a centralized meta-learning setting, we now extend this formulation to a federated learning scenario, which enables privacy-preserving, uncertainty-aware anomaly detection across distributed and heterogeneous clients. Compared to the centralized BayPrAnoMeta formulation in Section 3.1, the proposed federated extension introduces the following: (i) Training tasks are distributed across multiple clients, each holding local data that cannot be shared. Each client independently performs Bayesian inner-loop adaptation, and only model updates are communicated to the server; and (ii) While the Bayesian inner-loop adaptation remains identical to Section 3.1, the outer-loop objective is changed to incorporate a supervised contrastive regularization term in addition to the Bayesian query likelihood to mitigate representation drift caused by heterogeneous client data, which encourages globally consistent and discriminative embeddings.

**Federated episodic learning setup** We consider a federated learning setting with  $C$  clients, indexed by  $c \in \{1, \dots, C\}$ . Each client corresponds to an independent data source and retains its data locally. Learning proceeds episodically. At each communication round, client  $c$  samples a task  $\mathcal{T}_c \sim p(\mathcal{T})$  from its local data distribution and constructs an episode  $\mathcal{E}_c = (\mathcal{S}_c, \mathcal{Q}_c)$ , where  $\mathcal{S}_c$  denotes a small support set of normal samples and  $\mathcal{Q}_c$  denotes a query set containing labeled normal and anomalous samples.<sup>2</sup>

**Bayesian client-side inner-loop adaptation** Given the global meta-parameters  $\theta$  broadcast by the server, each client performs task-specific adaptation using the Bayesian Proto-MAML inner loop introduced in Section 3.1. For a support set  $\mathcal{S}_c$ , the Bayesian inner loss  $\mathcal{L}_{\text{inner}}^{\text{Bayes}}(\theta; \mathcal{S}_c)$  is defined as in Eq. (3). The adapted parameters are obtained via the one-step update  $\theta'_c = U(\theta; \mathcal{S}_c) = \theta - \alpha \nabla_{\theta} \mathcal{L}_{\text{inner}}^{\text{Bayes}}(\theta; \mathcal{S}_c)$ .

**Episode-level outer-loop objective** After inner-loop adaptation, each client evaluates an episode-level outer loss on its query set  $\mathcal{Q}_c$  using the adapted parameters  $\theta'_c$ . Following Section 3.1, the Bayesian query likelihood loss  $\mathcal{L}_{\text{query}}^{\text{Bayes}}(\theta'_c; \mathcal{S}_c, \mathcal{Q}_c)$  is computed using the Student- $t$  posterior predictive for normal samples and a fixed anomaly reference distribution. To improve representation quality across heterogeneous clients, we augment this objective with a supervised contrastive regularization term  $\mathcal{L}_{\text{supcon}}(\theta'_c; \mathcal{Q}_c)$ . The resulting episode-level loss is

$$\mathcal{L}(\theta; \mathcal{E}_c) = \mathcal{L}_{\text{query}}^{\text{Bayes}}(\theta'_c; \mathcal{S}_c, \mathcal{Q}_c) + \lambda \mathcal{L}_{\text{supcon}}(\theta'_c; \mathcal{Q}_c), \quad (6)$$

where  $\lambda > 0$  controls the strength of the contrastive regularization.

<sup>2</sup>Each client samples tasks locally; hence, in the federated setting, we index episodes directly by the client  $c$  and write  $\mathcal{E}_c = (\mathcal{S}_c, \mathcal{Q}_c)$ , with the underlying task index left implicit.

**Supervised contrastive loss.** Let  $z_i = f_{\theta_c}(x_i)$  denote the adapted embedding of a query sample  $(x_i, y_i) \in Q_c$ , with label  $y_i \in \{0, 1\}$  indicating normal or anomalous class. For each anchor  $i$ , define the positive index set  $P(i) = \{j \neq i \mid y_j = y_i\}$ . The supervised contrastive loss is given by

$$\mathcal{L}_{\text{supcon}} = \sum_i \frac{-1}{|P(i)|} \sum_{p \in P(i)} \log \frac{\exp(z_i^\top z_p / \tau)}{\sum_{k \neq i} \exp(z_i^\top z_k / \tau)}, \quad (7)$$

where  $\tau$  is the temperature parameter.

**Client and global objectives** Each client  $c$  induces an episode distribution  $\mathcal{D}_c$  through its local task and episode sampling procedure. The client-level objective is defined as

$$F_c(\theta) := \mathbb{E}_{\mathcal{E}_c \sim \mathcal{D}_c} [\mathcal{L}(\theta; \mathcal{E}_c)]. \quad (8)$$

The global federated meta-objective is the average of client objectives,

$$F(\theta) := \frac{1}{C} \sum_{c=1}^C F_c(\theta). \quad (9)$$

**Federated optimization and server-side aggregation** At round  $r$ , the server has  $\theta^{r-1}$  and selects a subset  $\mathcal{C}_r \subseteq \mathcal{C}$ . Each selected client draws an episode  $\mathcal{E}_c^r \sim \mathcal{D}_c$  and forms the stochastic meta-gradient  $g_c^r := \nabla_{\theta_c} \mathcal{L}(\theta^{r-1}; \mathcal{E}_c)$ . The server then aggregates

$$\bar{g}^r = \frac{1}{|\mathcal{C}_r|} \sum_{c \in \mathcal{C}_r} g_c^r, \quad \theta^r = \theta^{r-1} - \eta \bar{g}^r, \quad (10)$$

where  $\eta := \gamma \beta$  (server aggregation  $\times$  meta step size). This procedure is analyzed theoretically in the Appendix.

**Test-time anomaly detection** At test time, no contrastive regularization is used. For a previously unseen task, Bayesian inner-loop adaptation is performed using a small support set of normal samples, and anomaly scores are computed using the likelihood-ratio criterion defined in Section 3.1.

To conduct this experiment, we consider the object categories (like, *Bottle*, *Cable*, among others) of the MVTec AD dataset (Bergmann et al., 2019) as individual clients of the federated set-up. Here, we assume each client as an independent anomaly detection task. Each client corresponds to a distinct industrial object category and performs task-specific Bayesian Proto-MAML adaptation and supervised contrastive representation learning exclusively on its local data, which is never shared with the server. The client datasets are strongly non-i.i.d., differing in visual structure, anomaly subtypes, and class imbalance, and the server does not have access to a unified global objective or synchronized mini-batches. Instead, clients independently compute meta-gradients arising from episodic, task-conditioned objectives, and only these updates are communicated to the server, which performs aggregation without observing client losses, labels, or contrastive pairs. This separation between local task adaptation and global aggregation, combined with heterogeneous client objectives and privacy-preserving update exchange, fundamentally distinguishes our approach from distributed training and aligns it with the defining principles of federated learning. Moreover, we handle client heterogeneity implicitly through episodic meta-learning and Bayesian task-specific adaptation, which allows each client of the federated set-up to maintain probabilistic normality model while sharing only meta-level representations via federated aggregation. The algorithm of this setting is given in Algorithm 1, along with the proposed BayPrAnoMeta training and testing algorithm (Algorithms 2 and 3 respectively) in the Appendix.

In the next section, we provide an optimization-theoretic convergence guarantee for the federated training procedure in Algorithm 1. Our goal is to establish convergence to *stationary points* of the (nonconvex) global federated Bayesian meta-objective under standard smoothness, variance, and heterogeneity assumptions, and to make explicit the additional regularity conditions required by the NIW–Student- $t$  predictive likelihood.

## 4 Theoretical guarantees

**Assumptions.** The following conditions are standard in nonconvex stochastic/federated optimization and are stated here to make the guarantee precise. The expressions of the client objective and meta objective are as in (8) and (9) respectively.

**Assumption 2** (Smoothness of client objectives). Each  $F_c$  is  $L$ -smooth: for all  $\theta, \theta'$ ,

$$\|\nabla F_c(\theta) - \nabla F_c(\theta')\| \leq L \|\theta - \theta'\|.$$

Consequently,  $F$  is also  $L$ -smooth.

---

**Algorithm 1** Federated BayPrAnoMeta with Supervised Contrastive Learning

---

**Input:** Client set  $\mathcal{C}$ ; embedding network  $f_\theta$ ; NIW prior  $(\mu_0, \kappa_0, \Lambda_0, \nu_0)$ ; anomaly reference model  $p_1(z)$ ; temperature  $\tau$ ; regularization coefficient  $\lambda$ ; inner-loop step size  $\alpha$ ; meta step size  $\beta$ ; server aggregation rate  $\gamma$ ; number of rounds  $R$

**Output:** Global meta-parameters  $\theta^R$

**Initialize:**  $\theta^0$

**for**  $r = 1$  to  $R$  **do**

    Server broadcasts  $\theta^{r-1}$

**for all** clients  $c \in \mathcal{C}$  **in parallel do**

$\theta_c \leftarrow \theta^{r-1}$

        Sample an episode  $\mathcal{E}_c = (\mathcal{S}_c, \mathcal{Q}_c)$

**Bayesian inner loop:**

            Compute embeddings  $z_i = f_{\theta_c}(x_i)$  for  $x_i \in \mathcal{S}_c$

            Compute NIW posterior parameters  $(\mu_{n,c}, \Lambda_{n,c}, \kappa_{n,c}, \nu_{n,c})$

            Define Student- $t$  posterior predictive  $p_{0,\theta_c}(\cdot | \mathcal{S}_c)$

$\mathcal{L}_{\text{inner}}^{\text{Bayes}}(\theta_c; \mathcal{S}_c) = -\sum_{x_i \in \mathcal{S}_c} \log p_{0,\theta_c}(f_{\theta_c}(x_i) | \mathcal{S}_c)$

$\theta'_c \leftarrow U(\theta_c; \mathcal{S}_c) = \theta_c - \alpha \nabla_{\theta_c} \mathcal{L}_{\text{inner}}^{\text{Bayes}}(\theta_c; \mathcal{S}_c)$

**Outer loop:**

                Compute adapted query embeddings  $z_j = f_{\theta'_c}(x_j)$  for  $(x_j, y_j) \in \mathcal{Q}_c$

                Compute  $\mathcal{L}_{\text{query}}^{\text{Bayes}}(\theta'_c; \mathcal{S}_c, \mathcal{Q}_c)$  as in (5)

                Define  $P(i) = \{j \neq i : y_j = y_i\}$

                Compute  $\mathcal{L}_{\text{supcon}}(\theta'_c; \mathcal{Q}_c)$  as in (7)

$\mathcal{L}(\theta^{r-1}; \mathcal{E}_c) = \mathcal{L}_{\text{query}}^{\text{Bayes}}(\theta'_c; \mathcal{S}_c, \mathcal{Q}_c) + \lambda \mathcal{L}_{\text{supcon}}(\theta'_c; \mathcal{Q}_c)$

$g_c^r \leftarrow \nabla_{\theta_c} \mathcal{L}(\theta^{r-1}; \mathcal{E}_c)$

                Send  $g_c^r$  to server

**end for**

**Server aggregation:**

$\bar{g}^r = \frac{1}{|\mathcal{C}|} \sum_{c \in \mathcal{C}} g_c^r$ ,  $\eta \leftarrow \gamma \beta$ ,  $\theta^r = \theta^{r-1} - \eta \bar{g}^r$

**end for**

**Test-time:**

        Given a new episode  $\mathcal{E} = (\mathcal{S}, \mathcal{Q})$ , compute  $\theta' = U(\theta^R; \mathcal{S})$

        For a test sample  $x^*$ , output anomaly score

$s(x^*) = \log p_1(f_{\theta'}(x^*)) - \log p_{0,\theta'}(f_{\theta'}(x^*) | \mathcal{S})$

---

**Assumption 3** (Unbiased stochastic meta-gradients and bounded variance). For each round  $r$  and selected client  $c \in \mathcal{C}_r$ ,

$$\mathbb{E}[g_c^r | \theta^r] = \nabla F_c(\theta^r), \quad \mathbb{E}[\|g_c^r - \nabla F_c(\theta^r)\|^2 | \theta^r] \leq \sigma^2.$$

**Assumption 4** (Bounded client heterogeneity). There exists  $\zeta \geq 0$  such that for all  $\theta$ ,

$$\frac{1}{|\mathcal{C}|} \sum_{c \in \mathcal{C}} \|\nabla F_c(\theta) - \nabla F(\theta)\|^2 \leq \zeta^2.$$

**Assumption 5** (Predictive regularity (NIW–Student- $t$  well-posedness)). There exists  $\varepsilon > 0$  such that the predictive scale matrices satisfy, for all  $\theta$  and all support sets  $\mathcal{S}$  with  $|\mathcal{S}| = K$ ,

$$\Sigma_n \succeq \varepsilon I_d.$$

Under the NIW prior with  $\Lambda_0 \succ 0$  and  $\nu_0 > d - 1$ , the predictive scale  $\Sigma_n$  is strictly positive definite for all  $K \geq 1$  (Proposition A.7), so Assumption 5 holds automatically. Additionally, this prevents singular covariance estimates when  $K < d$  (few-shot regime), and it ensures the Student- $t$  log-likelihood has bounded curvature.

**Lemma 1** (Smoothness of Student- $t$  negative log-likelihood in the embedding). Fix  $\nu > 0$ ,  $\mu \in \mathbb{R}^d$ , and a symmetric  $\Sigma \succeq \varepsilon I_d$ . Let

$$\ell(z) := -\log \text{Student-}t(z | \mu, \Sigma, \nu), \quad z \in \mathbb{R}^d.$$

Then  $\ell$  is twice differentiable and has a globally bounded Hessian on any bounded set  $\{z : \|z - \mu\| \leq R_z\}$ . In particular, for all  $\|z - \mu\| \leq R_z$ ,

$$\begin{aligned} \|\nabla^2 \ell(z)\| &\leq \frac{\nu + d}{\nu} \|\Sigma^{-1}\| + \frac{2(\nu + d)}{\nu^2} \|\Sigma^{-1}\|^2 R_z^2 \\ &\leq \frac{\nu + d}{\nu} \frac{1}{\varepsilon} + \frac{2(\nu + d)}{\nu^2} \frac{R_z^2}{\varepsilon^2}. \end{aligned}$$

Consequently,  $\nabla \ell$  is Lipschitz on  $\{z : \|z - \mu\| \leq R_z\}$ , with Lipschitz constant equal to the bound above.

Table 1: AUROC (%) across MVTec AD object categories for several baselines.

Category	PatchCore-25	Classical MAML	Classical Proto-MAML	BayPrAnoMeta	Better Performance?
Bottle	<b>100.0 ± 0.00</b>	27.5 ± 0.90	98.0 ± 0.14	98.4 ± 0.13	✗
Cable	50.8 ± 0.79	58.4 ± 0.83	95.7 ± 0.30	<b>96.9 ± 0.23</b>	✓
Capsule	<b>68.9 ± 0.56</b>	51.6 ± 0.99	61.8 ± 0.86	67.9 ± 0.76	✗
Carpet	47.6 ± 0.63	75.8 ± 0.90	89.5 ± 0.57	<b>93.7 ± 0.45</b>	✓
Grid	42.6 ± 0.80	62.6 ± 0.69	57.7 ± 0.87	<b>67.9 ± 0.79</b>	✓
Hazelnut	43.7 ± 0.57	61.5 ± 0.98	66.7 ± 0.81	<b>75.0 ± 0.74</b>	✓
Leather	36.5 ± 0.67	44.4 ± 1.15	85.5 ± 0.60	<b>89.5 ± 0.50</b>	✓
Metal Nut	53.2 ± 0.63	38.1 ± 0.94	84.4 ± 0.75	<b>85.8 ± 0.67</b>	✓
Pill	44.6 ± 0.54	60.1 ± 1.06	60.9 ± 0.85	<b>65.8 ± 0.80</b>	✓
Screw	56.0 ± 0.55	45.9 ± 0.78	50.1 ± 0.87	<b>57.6 ± 0.76</b>	✓
Tile	53.0 ± 0.60	95.6 ± 0.35	98.4 ± 0.13	<b>99.5 ± 0.07</b>	✓
Transistor	63.8 ± 0.97	64.1 ± 0.96	81.0 ± 0.61	<b>84.4 ± 0.57</b>	✓
Wood	54.3 ± 0.90	64.8 ± 0.86	99.2 ± 0.10	<b>99.6 ± 0.05</b>	✓
Zipper	65.4 ± 0.63	59.8 ± 0.96	93.7 ± 0.38	<b>95.0 ± 0.32</b>	✓

**Implication for BayPrAnoMeta.** Under Assumption 5 and bounded embeddings within episodes, Lemma 1 implies the Student- $t$  likelihood terms in (2)–(5) are smooth in the embedding  $z$ . Together with standard smoothness of  $f_\theta$  (bounded Jacobian/Hessian on the parameter domain traversed by training), this yields smoothness of the composed losses in  $\theta$ , supporting Assumption 2.

We now state a standard nonconvex convergence guarantee for the federated update (10). The result is stated in terms of stationarity of the global objective  $F$ .

**Theorem 6** (Nonconvex convergence of Federated BayPrAnoMeta). *Suppose Assumptions 2–5 hold. Let  $\{\theta^r\}_{r \geq 0}$  be generated by (10), where at each round the client subset  $\mathcal{C}_r$  is sampled uniformly without bias (or  $\mathcal{C}_r = \mathcal{C}$ ). Assume  $\eta \leq 1/L$ . Then, for any  $R \geq 1$ ,*

$$\begin{aligned} \frac{1}{R} \sum_{r=0}^{R-1} \mathbb{E}[\|\nabla F(\theta^r)\|^2] &\leq \frac{2(F(\theta^0) - F^*)}{\eta R} \\ &\quad + L\eta \left( \frac{\sigma^2}{|\mathcal{C}_r|} + \zeta^2 \right). \end{aligned} \tag{11}$$

where  $F^* := \inf_\theta F(\theta)$ . In particular, choosing  $\eta = \Theta(R^{-1/2})$  yields

$$\min_{0 \leq r \leq R-1} \mathbb{E}[\|\nabla F(\theta^r)\|^2] = \mathcal{O}\left(\frac{1}{\sqrt{R}}\right) + \mathcal{O}\left(\frac{\sigma^2}{|\mathcal{C}_r|}\right) + \mathcal{O}(\zeta^2).$$

Theorem 6 establishes that Federated BayPrAnoMeta converges to an  $\varepsilon$ -stationary point of the global objective  $F$  at the standard nonconvex stochastic rate, up to two unavoidable error sources: (i) episode-level stochasticity  $\sigma^2$ , reduced by larger client participation  $|\mathcal{C}_r|$ , and (ii) non-IID client heterogeneity  $\zeta^2$ . Also, the regularity of the predictive scale matrix is precisely what permits differentiable inner-loop adaptation and the application of standard nonconvex federated optimization arguments to our Bayesian meta-learning objective. The novelty lies not in the convergence rate per se, but in showing that Bayesian inner-loop adaptation with heavy-tailed predictive likelihoods satisfies the smoothness conditions required for federated meta-optimization.

## 5 Results and Discussion

Table 1 compares the proposed BayPrAnoMeta (Bayesian Proto-MAML) with several baselines: PatchCore (Roth et al., 2022), classical MAML (Finn et al., 2017), and Proto-MAML (Alfatemi et al., 2025). To ensure a fair architectural comparison, all methods operate under a shared representation constraint. Specifically, PatchCore is adapted to use the same 128-dimensional ResNet-18 projection head as BayPrAnoMeta, rather than its original multi-scale, high-dimensional feature hierarchy. Patch representations are obtained via dense feature extraction using this shared encoder, followed by k-center subsampling (25%) for efficiency and nearest-neighbor scoring. This constrained version intentionally omits multi-layer feature aggregation, which is known to benefit PatchCore, and therefore may reduce its absolute performance. However, this design ensures that performance differences reflect inference strategy—Bayesian

Table 2: AUROC (%) comparison across MVTec AD object categories for ablation studies.

Category	Contrastive BayPrAnoMeta	Federated BayPrAnoMeta	Federated Contrastive BayPrAnoMeta
Bottle	$49.0 \pm 1.94$	$88.7 \pm 0.73$	<b><math>88.9 \pm 0.75</math></b>
Cable	<b><math>93.6 \pm 0.45</math></b>	$59.4 \pm 1.02$	$58.8 \pm 1.03$
Capsule	$55.4 \pm 1.00$	<b><math>68.9 \pm 0.95</math></b>	$63.8 \pm 1.07$
Carpet	<b><math>53.0 \pm 1.21</math></b>	$45.4 \pm 1.32$	$52.3 \pm 1.22$
Grid	<b><math>65.3 \pm 0.88</math></b>	$59.7 \pm 0.97$	$59.1 \pm 0.90$
Hazelnut	$75.1 \pm 0.80$	$80.9 \pm 0.84$	<b><math>82.4 \pm 0.79</math></b>
Leather	$47.2 \pm 1.69$	$55.9 \pm 1.09$	<b><math>59.7 \pm 1.13</math></b>
Metal Nut	<b><math>76.2 \pm 0.96</math></b>	$70.8 \pm 0.83$	$72.0 \pm 0.78$
Pill	$55.2 \pm 1.08$	<b><math>57.8 \pm 0.98</math></b>	$51.9 \pm 0.98$
Screw	$54.9 \pm 0.81$	<b><math>63.1 \pm 1.16</math></b>	$46.1 \pm 1.17$
Tile	$39.4 \pm 1.61$	<b><math>56.9 \pm 1.08</math></b>	$52.2 \pm 1.14$
Transistor	<b><math>67.8 \pm 0.94</math></b>	$41.8 \pm 1.08$	$43.1 \pm 1.10$
Wood	$62.6 \pm 1.44$	$67.8 \pm 1.63$	<b><math>75.7 \pm 1.42</math></b>
Zipper	$71.3 \pm 1.19$	$72.9 \pm 1.20$	<b><math>84.8 \pm 0.92</math></b>

meta-learning and uncertainty-aware scoring—rather than representation capacity or feature specialization. PatchCore is trained exclusively on normal samples from the held-out test split, following the same episodic protocol used for the meta-learning baselines.

PatchCore exhibits strong performance on visually homogeneous and texture-simple objects such as *Bottle*, where anomalies are highly separable at the local patch level. However, its performance degrades on structurally complex categories including *Carpet*, *Grid*, *Leather*, and *Hazelnut*, where local patch statistics alone are less effective at capturing higher-level semantic or global shape deviations. In contrast, BayPrAnoMeta consistently outperforms PatchCore across most object categories, particularly those involving global shape irregularities or high intra-class variability. PatchCore results are reported at 25% coreset, with additional configurations (1%, 10%, 50%, 100%) provided in Appendix G. These results indicate that while PatchCore remains a strong baseline, BayPrAnoMeta offers a more robust, uncertainty-aware, and task-adaptive approach to few-shot anomaly detection.

Classical MAML performs poorly across object categories (Table 1), likely due to its reliance on discriminative gradient-based adaptation. Incorporating prototypical networks into MAML reframes task adaptation as a metric-learning problem, enabling the learning of compact representations of normal samples. This hybrid Proto-MAML formulation significantly improves anomaly detection performance across heterogeneous object categories, emphasizing the role of representation-based adaptation in few-shot settings.

Building upon Proto-MAML, Table 1 shows that Bayesian Proto-MAML (BayPrAnoMeta) further improves detection accuracy by modeling normal embeddings probabilistically and using likelihood-based anomaly scoring. This probabilistic treatment is particularly effective for challenging object categories with high intra-class variability, leading to the best performance in 12 out of 14 categories. The gains are most pronounced on structurally complex objects such as *Grid* (+10.2 AUROC), *Hazelnut* (+8.3), and *Carpet* (+4.2), while performance remains comparable on visually simpler categories such as *Bottle* and *Capsule*. These results indicate that Bayesian uncertainty modeling is especially beneficial in challenging, high intra-class variability settings.

## 5.1 Ablation Experiment

Table 2 compares Contrastive BayPrAnoMeta, Federated BayPrAnoMeta, and Federated Contrastive BayPrAnoMeta. Incorporating supervised contrastive learning in the federated setting improves anomaly detection for several visually structured and texture-rich categories, including *Bottle*, *Hazelnut*, *Leather*, *Wood*, and *Zipper*. Notably, Federated Contrastive BayPrAnoMeta achieves substantial gains on *Zipper* (+11.9 AUROC), *Wood* (+7.9), and *Leather* (+3.8) compared to its non-contrastive federated counterpart.

While improvements are not uniform across all categories (e.g., *Cable*, *Screw*, and *Pill*), this behavior is expected in few-shot anomaly detection, where contrastive objectives may over-regularize the embedding space when anomaly subtypes are scarce or visually similar. Overall, the results suggest that contrastive supervision acts as a representation stabilizer under client heterogeneity, leading to more robust anomaly scoring when supervision is distributed across heterogeneous clients.

## 6 Conclusion

In this paper, we propose BayPrAnoMeta, a Bayesian extension of Proto-MAML for few-shot industrial anomaly detection. Our method replaces deterministic prototypes with Normal-Inverse-Wishart (NIW) prior to model class conditional embeddings. This change enables uncertainty-aware task adaptation and a principled, likelihood-based approach to anomaly scoring. We conduct extensive experiments on the MVTec AD dataset, which show that BayPrAnoMeta consistently outperforms both classical MAML and Proto-MAML across most object categories, demonstrating particular efficacy with challenging texture-based anomalies. Although contrastive learning degrades performance in centralized settings, we find that supervised contrastive regularization is beneficial in federated environments with strong client heterogeneity. This finding suggests that contrastive objectives primarily function to align client-specific representations during the aggregation process, rather than simply improving individual discrimination. In summary, our results establish Bayesian Proto-MAML as a robust meta-learning framework for industrial anomaly detection, which offers a principled methodology for combining Bayesian inference, meta-learning, and federated optimization in environments where data are scarce and highly heterogeneous.

## References

Alfatemi, A., Rahouti, M., Bhuiyan, Z. A., Solyman, A., and Aledhari, M. (2025). Protomaml: A hybrid meta-learning approach integrating prototypical networks for data-efficient ddos attack detection. In *2025 International Wireless Communications and Mobile Computing (IWCMC)*, pages 1144–1149. IEEE.

Bergmann, P., Fauser, M., Sattlegger, D., and Steger, C. (2019). Mvtac ad—a comprehensive real-world dataset for unsupervised anomaly detection. In *Proceedings of the IEEE/CVF conference on computer vision and pattern recognition*, pages 9592–9600.

Chen, F., Luo, M., Dong, Z., Li, Z., and He, X. (2018). Federated meta-learning with fast convergence and efficient communication. *arXiv preprint arXiv:1802.07876*.

Defard, T., Setkov, A., Loesch, A., and Audigier, R. (2021). Padim: a patch distribution modeling framework for anomaly detection and localization. In *International conference on pattern recognition*, pages 475–489. Springer.

Fallah, A., Mokhtari, A., and Ozdaglar, A. (2020). Personalized federated learning with theoretical guarantees: A model-agnostic meta-learning approach. In *Advances in Neural Information Processing Systems*.

Finn, C., Abbeel, P., and Levine, S. (2017). Model-agnostic meta-learning for fast adaptation of deep networks. In *International conference on machine learning*, pages 1126–1135. PMLR.

Gordon, J., Bronskill, J., Bauer, M., Nowozin, S., and Turner, R. E. (2018). Meta-learning probabilistic inference for prediction. *arXiv preprint arXiv:1805.09921*.

Grant, E., Finn, C., Levine, S., Darrell, T., and Griffiths, T. L. (2018). Recasting gradient-based meta-learning as hierarchical bayes. In *International Conference on Learning Representations*.

Hospedales, T., Antoniou, A., Micaelli, P., and Storkey, A. (2021). Meta-learning in neural networks: A survey. *IEEE transactions on pattern analysis and machine intelligence* 1.

Kairouz, P., McMahan, H. B., Avent, B., Bellet, A., Bennis, M., Bhagoji, A. N., Bonawitz, K., Charles, Z., Cormode, G., Cummings, R., et al. (2021). Advances and open problems in federated learning. *Foundations and trends® in machine learning*, 14(1–2):1–210.

Khosla, P., Teterwak, P., Wang, C., Sarna, A., Tian, Y., Isola, P., Maschinot, A., Liu, C., and Krishnan, D. (2020). Supervised contrastive learning. *Advances in neural information processing systems*, 33:18661–18673.

Langley, P. (2000). Crafting papers on machine learning. In Langley, P., editor, *Proceedings of the 17th International Conference on Machine Learning (ICML 2000)*, pages 1207–1216, Stanford, CA. Morgan Kaufmann.

Li, Z., Yan, Y., Wang, X., Ge, Y., and Meng, L. (2025). A survey of deep learning for industrial visual anomaly detection. *Artificial Intelligence Review*, 58(9):279.

Liang, Y., Zhang, J., Zhao, S., Wu, R., Liu, Y., and Pan, S. (2023). Omni-frequency channel-selection representations for unsupervised anomaly detection. *IEEE Transactions on Image Processing*, 32:4327–4340.

Malinin, A. and Gales, M. (2018). Predictive uncertainty estimation via prior networks. *Advances in neural information processing systems*, 31.

McMahan, B., Moore, E., Ramage, D., Hampson, S., and y Arcas, B. A. (2017). Communication-efficient learning of deep networks from decentralized data. In *Artificial intelligence and statistics*, pages 1273–1282. PMLR.

Murphy, K. P. (2012). *Machine learning: a probabilistic perspective*. MIT press.

Pang, G., Shen, C., Cao, L., and Hengel, A. V. D. (2021). Deep learning for anomaly detection: A review. *ACM computing surveys (CSUR)*, 54(2):1–38.

Roth, K., Pemula, L., Zepeda, J., Schölkopf, B., Brox, T., and Gehler, P. (2022). Towards total recall in industrial anomaly detection. In *Proceedings of the IEEE/CVF Conference on Computer Vision and Pattern Recognition (CVPR)*, pages 14318–14328.

Ruff, L., Vandermeulen, R., Goernitz, N., Deecke, L., Siddiqui, S. A., Binder, A., Müller, E., and Kloft, M. (2018). Deep one-class classification. In *International conference on machine learning*, pages 4393–4402. PMLR.

Snell, J., Swersky, K., and Zemel, R. (2017). Prototypical networks for few-shot learning. *Advances in neural information processing systems*, 30.

Sung, F., Yang, Y., Zhang, L., Xiang, T., Torr, P. H., and Hospedales, T. M. (2018). Learning to compare: Relation network for few-shot learning. In *Proceedings of the IEEE Conference on Computer Vision and Pattern Recognition*, pages 1199–1208.

Tien, T. D., Nguyen, A. T., Tran, N. H., Huy, T. D., Duong, S., Nguyen, C. D. T., and Truong, S. Q. (2023). Revisiting reverse distillation for anomaly detection. In *Proceedings of the IEEE/CVF conference on computer vision and pattern recognition*, pages 24511–24520.

Vinyals, O., Blundell, C., Lillicrap, T., Kavukcuoglu, K., and Wierstra, D. (2016). Matching networks for one shot learning. In *Advances in Neural Information Processing Systems*.

## Appendices

The appendices provide additional methodological, algorithmic, and theoretical details that complement the main text and are included to ensure clarity and reproducibility.

### A Classical Proto-MAML for few-shot anomaly detection

**Motivation** In modern manufacturing environments, visual anomaly detection systems are expected to identify subtle defects such as scratches, dents, misalignments, and contaminations before they propagate downstream and cause costly failures. Unlike conventional classification problems, these defects are inherently rare, visually diverse, and often unknown at deployment time. As a result, collecting large, well-balanced, and exhaustively labeled datasets of all possible defect types is practically infeasible. This setting naturally violates the assumptions of classical supervised learning and motivates few-shot learning formulations.

Few-shot anomaly detection can be naturally framed as a meta-learning problem, where each task corresponds to learning a normality model from a small number of examples and detecting deviations from it. In prototypical networks, each task is represented by a prototype computed as the mean of support embeddings, and query samples are classified based on their distance from this prototype (Snell et al., 2017). When applied to anomaly detection, the support set typically contains only normal samples, and anomalies are identified as samples whose embeddings lie far from the normal prototype in the learned metric space. This paradigm has been widely adopted in industrial anomaly detection, particularly on datasets such as MVTec AD, due to its simplicity and effectiveness under limited supervision (Bergmann et al., 2019; Ruff et al., 2018; Pang et al., 2021).

Proto-MAML, a hybridization of prototypical networks and model-agnostic meta-learning (MAML), extends this idea by incorporating task-specific adaptation through gradient-based meta-learning (Finn et al., 2017). In this formulation, the embedding network is meta-trained such that a small number of gradient steps on the support set minimizes the dispersion of normal embeddings around their prototype. After adaptation, anomaly scores for query samples are computed using distance-based metrics in the adapted embedding space that enables rapid adaptation to new object categories.

Despite its success, classical Proto-MAML for anomaly detection has certain limitations. First, the prototype is treated as a point estimate, ignoring uncertainty arising from small support sets. Second, Euclidean distance-based scoring lacks probabilistic interpretability. Finally, discriminative objectives dominate the learning process, providing limited uncertainty quantification—an essential requirement in safety-critical industrial systems (Malinin and Gales, 2018).

These limitations motivate a probabilistic reformulation of Proto-MAML, where normality is modeled as a distribution rather than a point, and anomaly detection is performed using likelihood-based inference. In the following section, we introduce BayPrAnoMeta, a Bayesian extension of Proto-MAML that addresses these shortcomings while preserving its few-shot adaptability. We study few-shot industrial anomaly detection under a meta-learning framework.

**Prototype estimation** Given support embeddings  $z_i = f_\theta(x_i)$ , the task-specific prototype is computed as

$$c\mathcal{T} = \frac{1}{K} \sum_{i=1}^K z_i.$$

**Inner-loop adaptation** Proto-MAML adapts the embedding network by minimizing the dispersion of support embeddings around the prototype:

$$\mathcal{L}_{\text{inner}}(\theta; \mathcal{S}_{\mathcal{T}}) = \frac{1}{K} \sum_{i=1}^K \|f_\theta(x_i) - c\mathcal{T}\|_2^2.$$

The task-adapted parameters are obtained via one or more gradient descent steps:  $\theta_{\mathcal{T}} = \theta - \alpha \nabla_{\theta} \mathcal{L}_{\text{inner}}(\theta; \mathcal{S}_{\mathcal{T}})$ .

**Query scoring** For a query sample  $x_j$ , the adapted embedding  $z_j = f_{\theta_{\mathcal{T}}}(x_j)$  is compared to the prototype using squared Euclidean distance. The anomaly logit is defined as:  $\ell_j = -\|z_j - c\mathcal{T}\|_2^2$ .

**Outer-loop meta-objective** Given labels  $y_j \in \{0, 1\}$ , the query loss is defined using binary cross-entropy with logits:

$$\mathcal{L}_{\text{query}} = \sum_j \text{BCEWithLogits}(\ell_j, y_j),$$

which is equivalent to

$$\mathcal{L}_{\text{query}} = - \sum_j [y_j \log \sigma(\ell_j) + (1 - y_j) \log(1 - \sigma(\ell_j))],$$

where  $\sigma(\cdot)$  denotes the sigmoid function. The meta-learning objective minimizes the expected query loss across tasks:

$$\min_{\theta} \mathbb{E}_{\mathcal{T} \sim p(\mathcal{T})} [\mathcal{L}_{\text{query}}(\theta_{\mathcal{T}})],$$

with gradients propagated through the inner-loop update, and the meta-parameters updated using gradient descent with meta-learning rate  $\beta$ :

$$\theta \leftarrow \theta - \beta \nabla_{\theta} \mathbb{E}_{\mathcal{T} \sim p(\mathcal{T})} [\mathcal{L}_{\text{query}}(\theta_{\mathcal{T}})].$$

**Testing and anomaly detection** At test time, for a previously unseen task  $\mathcal{T}$ , a support set  $\mathcal{S}_{\mathcal{T}}$  consisting only of normal samples is provided. The prototype  $c_{\mathcal{T}}$  is computed from the support embeddings, and the embedding network is adapted via the Proto-MAML inner loop to obtain  $\theta_{\mathcal{T}}$ . For a test sample  $x^*$ , the anomaly score is defined as

$$s(x^*) = \|f_{\theta_{\mathcal{T}}}(x^*) - c_{\mathcal{T}}\|_2^2.$$

Samples with larger scores are considered more likely to be anomalous.

## B BayPrAnoMeta Algorithm

This appendix provides detailed algorithm for the Meta-training and meta-testing of BayPrAnoMeta, introduced in Section 3.1.

---

### Algorithm 2 BayPrAnoMeta (Bayesian Proto-MAML): Meta-Training

---

**Input:** Task distribution  $p(\mathcal{T})$ ; embedding network  $f_{\theta}$ ; NIW prior  $(\mu_0, \kappa_0, \Lambda_0, \nu_0)$ ; step sizes  $\alpha, \beta$   
**while** not converged **do**  
 Sample tasks  $\mathcal{T} \sim p(\mathcal{T})$   
**for** all tasks  $\mathcal{T}$  **do**  
 Sample episode  $(\mathcal{S}_{\mathcal{T}}, \mathcal{Q}_{\mathcal{T}})$   
 Compute embeddings  $z_i = f_{\theta}(x_i)$  for  $x_i \in \mathcal{S}_{\mathcal{T}}$   
 $\bar{z} = \frac{1}{K} \sum_i z_i$   
 $S_z = \sum_i (z_i - \bar{z})(z_i - \bar{z})^{\top}$   
 $\kappa_n = \kappa_0 + K$   
 $\nu_n = \nu_0 + K$   
 $\mu_n = \frac{\kappa_0 \mu_0 + K \bar{z}}{\kappa_n}$   
 $\Lambda_n = \Lambda_0 + S_z + \frac{\kappa_0 K}{\kappa_n} (\bar{z} - \mu_0)(\bar{z} - \mu_0)^{\top}$   
 Define  $p_0(z | \mathcal{S}_{\mathcal{T}}) = \text{Student-}t(\mu_n, \Lambda_n, \nu_n)$   
 $\mathcal{L}_{\text{inner}}^{\text{Bayes}} = - \sum_{x_i \in \mathcal{S}_{\mathcal{T}}} \log p_0(f_{\theta}(x_i))$   
 $\theta_{\mathcal{T}} = \theta - \alpha \nabla_{\theta} \mathcal{L}_{\text{inner}}^{\text{Bayes}}$   
**for** all  $(x_j, y_j) \in \mathcal{Q}_{\mathcal{T}}$  **do**  
 $z_j = f_{\theta_{\mathcal{T}}}(x_j)$   
 $\mathcal{L}_{\text{query}}^{\text{Bayes}} = -(1 - y_j) \log p_0(z_j) - y_j \log p_1(z_j)$   
**end for**  
**end for**  
 $\theta \leftarrow \theta - \beta \nabla_{\theta} \sum_{\mathcal{T}} \sum \mathcal{L}_{\text{query}}^{\text{Bayes}}$   
**end while**

---

---

**Algorithm 3** BayPrAnoMeta (Bayesian Proto-MAML): Meta-Testing

---

**Input:** Initialization  $\theta$ ; support set  $\mathcal{S}_T$ ; test sample  $x^*$ ; threshold  $\tau$   
 Compute embeddings  $z_i = f_\theta(x_i)$  for  $x_i \in \mathcal{S}_T$   
 $\bar{z} = \frac{1}{K} \sum_i z_i$   
 $S_z = \sum_i (z_i - \bar{z})(z_i - \bar{z})^\top$   
 $\kappa_n = \kappa_0 + K$   
 $\nu_n = \nu_0 + K$   
 $\mu_n = \frac{\kappa_0 \mu_0 + K \bar{z}}{\kappa_n}$   
 $\Lambda_n = \Lambda_0 + S_z + \frac{\kappa_0 K}{\kappa_n} (\bar{z} - \mu_0)(\bar{z} - \mu_0)^\top$   
 Define  $p_0(z | \mathcal{S}_T) = \text{Student-}t(\mu_n, \Lambda_n, \nu_n)$   
 $\mathcal{L}_{\text{inner}}^{\text{Bayes}} = -\sum_{x_i \in \mathcal{S}_T} \log p_0(f_\theta(x_i))$   
 $\theta_T = \theta - \alpha \nabla_\theta \mathcal{L}_{\text{inner}}^{\text{Bayes}}$   
 $z^* = f_{\theta_T}(x^*)$   
 $s(x^*) = \log p_1(z^*) - \log p_0(z^* | \mathcal{S}_T)$   
**if**  $s(x^*) > \tau$  **then**  
     **Anomaly**  
**else**  
     **Normal**  
**end if**

---

## C Proofs of results

This appendix provides the proofs of the proposition on the well-posedness of the Student- $t$  posterior predictive distribution as outlined in Proposition 1. We also provide the proofs of the smoothness lemma given in Lemma 1, and the main result on optimization-theoretic convergence guarantee for the federated training procedure in Algorithm 1 as given by Theorem 6.

*Proof of Proposition 1.* Fix  $K \geq 1$  and  $\mathcal{S}$ . Since  $S_z \succeq 0$  and  $(\bar{z} - \mu_0)(\bar{z} - \mu_0)^\top \succeq 0$ , the update (1) implies

$$\Lambda_n = \Lambda_0 + \underbrace{S_z}_{\succeq 0} + \underbrace{\frac{\kappa_0 K}{\kappa_0 + K} (\bar{z} - \mu_0)(\bar{z} - \mu_0)^\top}_{\succeq 0} \succeq \Lambda_0 \succ 0.$$

Hence  $\Lambda_n$  is positive definite. Because  $\kappa_n = \kappa_0 + K > 0$  and  $\nu_{\text{pred}} = \nu_0 + K - d + 1 > 0$  by assumption, the scalar factor in  $\Sigma_n$  strictly positive. Therefore  $\Sigma_n$  is positive definite, proving (i).

A multivariate Student- $t$  distribution with degrees of freedom  $\nu_{\text{pred}} > 0$  and scale  $\Sigma_n \succ 0$  is a proper density on  $\mathbb{R}^d$ , and its log-density is finite everywhere, proving (ii).

□

**Corollary 7.** *The predictive scale is uniformly bounded below as*

$$\Sigma_n \succeq \frac{\kappa_n + 1}{\kappa_n(\nu_n - d + 1)} \Lambda_0 \succeq \frac{1}{\nu_0 + K - d + 1} \Lambda_0.$$

*Proof.* For the lower bound, since  $\Lambda_n \succeq \Lambda_0$ , multiplying by the positive scalar  $\frac{\kappa_n + 1}{\kappa_n(\nu_n - d + 1)}$  yields

$$\Sigma_n = \frac{\kappa_n + 1}{\kappa_n(\nu_n - d + 1)} \Lambda_n \succeq \frac{\kappa_n + 1}{\kappa_n(\nu_n - d + 1)} \Lambda_0.$$

Finally, observe that  $\frac{\kappa_n + 1}{\kappa_n} \geq 1$ , so

$$\frac{\kappa_n + 1}{\kappa_n(\nu_n - d + 1)} \geq \frac{1}{\nu_n - d + 1} = \frac{1}{\nu_0 + K - d + 1}.$$

□

**Corollary 8.** *Under the conditions of Proposition 1, Assumption 5 holds with  $\varepsilon = \lambda_{\min}(\Lambda_0)/(\nu_0 + K - d + 1)$ . Also, the uniform lower bound in Corollary 7 implies a uniform upper bound on the inverse scale:*

$$\|\Sigma_n^{-1}\| \leq \left( \frac{\nu_0 + K - d + 1}{\lambda_{\min}(\Lambda_0)} \right),$$

where  $\lambda_{\min}(\Lambda_0) > 0$  is the minimum eigenvalue of  $\Lambda_0$ .

Combined with Lemma 1, this shows that curvature and gradient Lipschitz constants of the Bayesian likelihood terms remain controlled in the few-shot regime because the prior prevents degeneracy of the predictive scale matrix.

*Proof of Lemma 1.* Let  $\delta(z) = (z - \mu)^\top \Sigma^{-1}(z - \mu)$ . Up to an additive constant, the Student- $t$  negative log-likelihood has the form

$$\ell(z) = \frac{\nu + d}{2} \log \left( 1 + \frac{1}{\nu} \delta(z) \right) + \text{const.}$$

A direct calculation yields

$$\nabla \ell(z) = \frac{\nu + d}{\nu + \delta(z)} \Sigma^{-1}(z - \mu),$$

and

$$\nabla^2 \ell(z) = \frac{\nu + d}{\nu + \delta(z)} \Sigma^{-1} - \frac{2(\nu + d)}{(\nu + \delta(z))^2} \Sigma^{-1}(z - \mu)(z - \mu)^\top \Sigma^{-1}.$$

Since  $\delta(z) \geq 0$ , we have  $(\nu + \delta(z))^{-1} \leq \nu^{-1}$  and  $(\nu + \delta(z))^{-2} \leq \nu^{-2}$ . On the set  $\|z - \mu\| \leq R_z$ ,

$$\|\Sigma^{-1}(z - \mu)(z - \mu)^\top \Sigma^{-1}\| \leq \|\Sigma^{-1}\|^2 \|z - \mu\|^2 \leq \|\Sigma^{-1}\|^2 R_z^2.$$

Combining these bounds gives the stated Hessian norm bound. The final inequality uses  $\|\Sigma^{-1}\| \leq 1/\varepsilon$  when  $\Sigma \succeq \varepsilon I_d$ .  $\square$

*Proof of Theorem 6.* Because  $F$  is  $L$ -smooth (Assumption 2), for any update  $\theta^{r+1} = \theta^r - \eta \bar{g}^r$  we have the descent inequality

$$F(\theta^{r+1}) \leq F(\theta^r) - \eta \langle \nabla F(\theta^r), \bar{g}^r \rangle + \frac{L\eta^2}{2} \|\bar{g}^r\|^2. \quad (12)$$

Take conditional expectation given  $\theta^r$ . By Assumption 3 and unbiased client sampling,  $\mathbb{E}[\bar{g}^r \mid \theta^r] = \nabla F(\theta^r)$ , hence

$$\mathbb{E}[\langle \nabla F(\theta^r), \bar{g}^r \rangle \mid \theta^r] = \|\nabla F(\theta^r)\|^2.$$

Moreover,

$$\mathbb{E}[\|\bar{g}^r\|^2 \mid \theta^r] = \|\nabla F(\theta^r)\|^2 + \mathbb{E}[\|\bar{g}^r - \nabla F(\theta^r)\|^2 \mid \theta^r].$$

Decompose the deviation as

$$\bar{g}^r - \nabla F(\theta^r) = \underbrace{\frac{1}{|\mathcal{C}_r|} \sum_{c \in \mathcal{C}_r} (g_c^r - \nabla F_c(\theta^r))}_{\text{stochastic episode noise}} + \underbrace{\frac{1}{|\mathcal{C}_r|} \sum_{c \in \mathcal{C}_r} (\nabla F_c(\theta^r) - \nabla F(\theta^r))}_{\text{client heterogeneity}}.$$

Using  $\|a + b\|^2 \leq 2\|a\|^2 + 2\|b\|^2$ , Jensen's inequality, and Assumptions 3–4, we obtain

$$\mathbb{E}[\|\bar{g}^r - \nabla F(\theta^r)\|^2 \mid \theta^r] \leq \frac{\sigma^2}{|\mathcal{C}_r|} + \zeta^2.$$

Substituting these bounds into (12) and taking total expectation gives

$$\mathbb{E}[F(\theta^{r+1})] \leq \mathbb{E}[F(\theta^r)] - \eta \left( 1 - \frac{L\eta}{2} \right) \mathbb{E}\|\nabla F(\theta^r)\|^2 + \frac{L\eta^2}{2} \left( \frac{\sigma^2}{|\mathcal{C}_r|} + \zeta^2 \right).$$

For  $\eta \leq 1/L$ , we have  $1 - \frac{L\eta}{2} \geq \frac{1}{2}$ , hence

$$\frac{\eta}{2} \mathbb{E}\|\nabla F(\theta^r)\|^2 \leq \mathbb{E}[F(\theta^r)] - \mathbb{E}[F(\theta^{r+1})] + \frac{L\eta^2}{2} \left( \frac{\sigma^2}{|\mathcal{C}_r|} + \zeta^2 \right).$$

Summing over  $r = 0, \dots, R - 1$  telescopes:

$$\frac{\eta}{2} \sum_{r=0}^{R-1} \mathbb{E}\|\nabla F(\theta^r)\|^2 \leq F(\theta^0) - \mathbb{E}[F(\theta^R)] + \frac{L\eta^2 R}{2} \left( \frac{\sigma^2}{|\mathcal{C}_r|} + \zeta^2 \right).$$

Lower bound  $\mathbb{E}[F(\theta^R)] \geq F^*$  and divide by  $\eta R/2$  to obtain (11).  $\square$

## D Experimental Setup

**Implementation details** All methods are implemented in PyTorch, using the `higher` library for differentiable inner-loop optimization. Experiments are conducted on CPU.

**Dataset and task definition** We evaluate all methods on the MVTec Anomaly Detection (MVTec AD) dataset (Bergmann et al., 2019), which contains high-resolution industrial images from 15 object categories (e.g., *Bottle*, *Cable*, *Capsule*, *Grid*, among others). Each object category is treated as an independent meta-learning task  $\mathcal{T}$ , following standard practice in few-shot learning. Each category consists of: (i). a set of normal images provided under `train/good` and `test/good`, and (ii). multiple anomaly subtypes organized as subdirectories under `test/`. All images are resized to  $224 \times 224$  pixels and normalized using ImageNet mean and standard deviation.

**Episodic few-shot formulation** Learning proceeds episodically. For each task  $\mathcal{T}$ , an episode  $\mathcal{E}_{\mathcal{T}} = (\mathcal{S}_{\mathcal{T}}, \mathcal{Q}_{\mathcal{T}})$  is constructed as follows: (i.) **Support set**  $\mathcal{S}_{\mathcal{T}}$ :  $K = 5$  normal samples only, and (ii.) **Query set**  $\mathcal{Q}_{\mathcal{T}}$ :  $Q_N = 12$  normal samples and  $Q_A = 4$  anomalous samples. Query labels are binary, with  $y = 0$  denoting normal samples and  $y = 1$  denoting anomalous samples. This episodic construction is used consistently during training, validation, and testing.

**Data preparation** To evaluate generalization to unseen anomaly types, we adopt the following data preparation protocol at the category level. For each object category: one anomaly subtype is held out entirely for testing, and all remaining anomaly subtypes are used during training. Specifically: (i). **Training**: normal samples from `train/good` and `test/good`, and anomalous samples from all but the held-out subtype. and (ii). **Testing**: normal samples from `test/good`, and anomalous samples exclusively from the held-out subtype. Categories with fewer than two anomaly subtypes (e.g., *toothbrush*) are excluded from our experiments. This data preparation ensures that anomaly types encountered at test time are strictly unseen during training.

### D.1 Model architecture

All methods share a common embedding network  $f_{\theta} : \mathcal{X} \rightarrow \mathbb{R}^{128}$ .

**Backbone** We use a ResNet-18 architecture initialized with ImageNet-pretrained weights. The final classification layer is removed, the first max-pooling layer is replaced with average pooling to preserve spatial detail, and global average pooling produces a 512-dimensional feature vector.

**Projection head** The backbone output is passed through a projection head consisting of a linear layer mapping  $512 \rightarrow 128$ , followed by a ReLU activation and Layer Normalization. The resulting 128-dimensional embedding is used for prototype estimation, Bayesian modeling, contrastive learning, and anomaly scoring.

**Meta-learning compatibility** The entire network, including both backbone and projection head, is optimized within a meta-learning framework. Gradients are propagated through task-specific inner-loop updates using differentiable optimization, enabling end-to-end meta-learning without task-specific classifier heads.

To ensure fair comparison, the same architecture is used unchanged across all baselines and proposed methods.

**Optimization and hyperparameters** Unless stated otherwise, all experiments use the hyperparameters listed in Table 3. Meta-optimization is performed using the Adam optimizer, and all random seeds are fixed to 42 for reproducibility.

Table 3: Optimization and training hyperparameters

Hyperparameter	Value
Inner-loop learning rate ( $\alpha$ )	$5 \times 10^{-4}$
Inner-loop steps	1
Meta-learning rate ( $\beta$ )	$1 \times 10^{-4}$
Episodes per epoch	50
Validation episodes per epoch	20
Training epochs / federated rounds	50
Server aggregation rate ( $\gamma$ )	1.0
Contrastive temperature ( $\tau$ )	0.07
Regularization coefficient ( $\lambda$ )	0.1
NIW prior mean ( $\mu_0$ )	$\mathbf{0} \in \mathbb{R}^{128}$
NIW prior mean strength ( $\kappa_0$ )	0.01
NIW prior scale matrix ( $\Lambda_0$ )	$I_{128}$
NIW prior degrees of freedom ( $\nu_0$ )	$128 + 2$
Anomaly reference mean ( $\mu_a$ )	$\mathbf{0} \in \mathbb{R}^{128}$
Anomaly reference covariance ( $\Sigma_a$ )	$100 \cdot I_{128}$
Anomaly reference degrees of freedom ( $\nu_a$ )	2

## D.2 Training and Validation

At each epoch, training loss is computed as the average meta-loss over 50 training episodes. Validation loss is computed over 20 validation episodes sampled from held-out data. Training and validation loss curves are reported to assess convergence and overfitting. The same set-up is used for centralized and federated model training.

**Evaluation metrics** At test time, anomaly scores are computed at the episode level and aggregated across episodes, i.e. All metrics are reported as mean  $\pm$  standard error over 300 randomly sampled test episodes. We report: Area Under the ROC (AUROC), Area Under the Precision-Recall (AUPRC), and F1-scores based on optimal threshold selected from the anomaly scores. Additionally, we obtain ROC curves, precision-recall curves, and score histograms, which we do not report in this paper for brevity. Details on computation of optimal threshold based F1-score is given in the next section (Section E).

## E F1 Score Computation (Optimal Threshold)

For each query sample  $x_j$ , the model produces a continuous anomaly score  $s_j \in \mathbb{R}$ , where larger values indicate higher anomaly likelihood. A threshold  $u$  maps scores to binary predictions

$$\hat{y}_j(u) = \begin{cases} 1, & s_j \geq u, \\ 0, & \text{otherwise.} \end{cases}$$

For each candidate threshold  $u$ , precision and recall are computed, yielding

$$\text{F1}(u) = \frac{2 \text{TP}(u)}{2 \text{TP}(u) + \text{FP}(u) + \text{FN}(u)}.$$

The optimal threshold is selected as  $u^* = \arg \max_u \text{F1}(u)$ , and the reported F1 score is  $\text{F1}^* = \text{F1}(u^*)$ , averaged across test episodes.

## F Discussions on Training and Validation Loss Curves

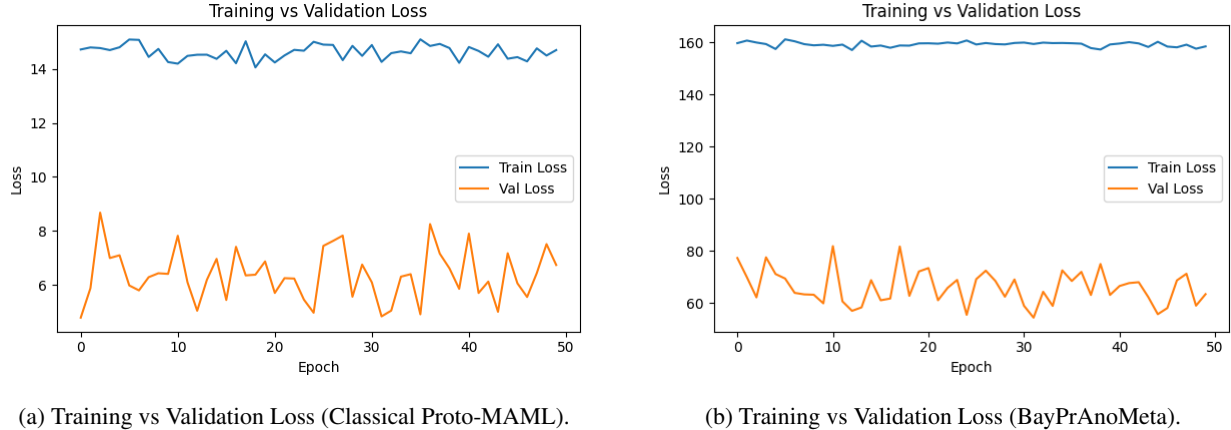


Figure 2: Comparison of training and validation loss curves of Classical Proto-MAML and BayPrAnoMeta (Bayesian Proto-MAML).

From Figure 2, it is clear that BayPrAnoMeta exhibits higher training loss values due to likelihood based optimization in high-dimensional embedding space its stable training and validation gap, and evaluation metrics indicate better and robust anomaly detection performance compared to Classical Proto-MAML. In episodic meta-learning, the training objective is evaluated over independently sampled tasks. Each episode induces its own support-set prototype (or Bayesian posterior), which causes the scale and difficulty of the loss to vary across episodes. As a result, optimization seeks a stable initialization that performs well on average across tasks, leading to convergence toward a stationary meta-loss rather than a monotonically decreasing training curve.

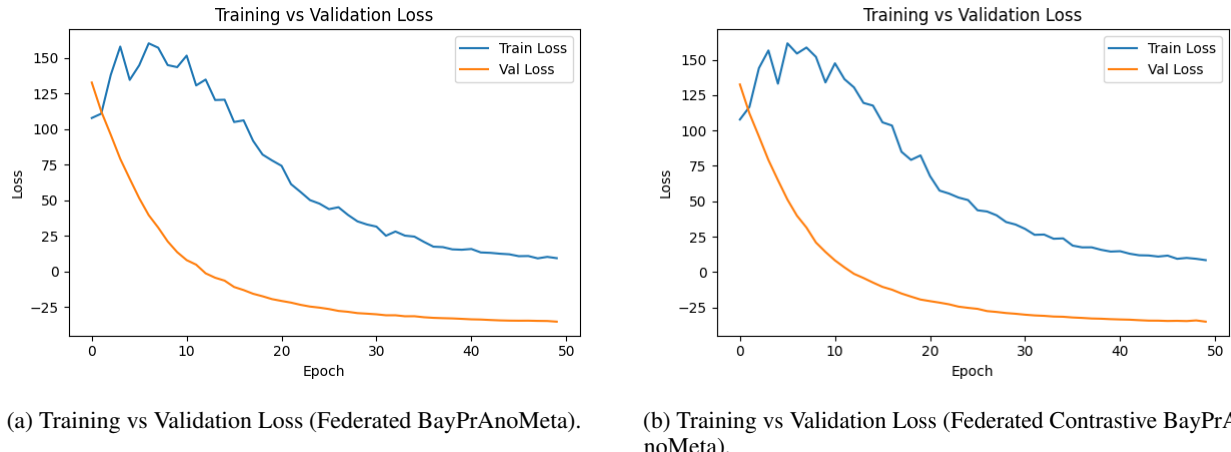
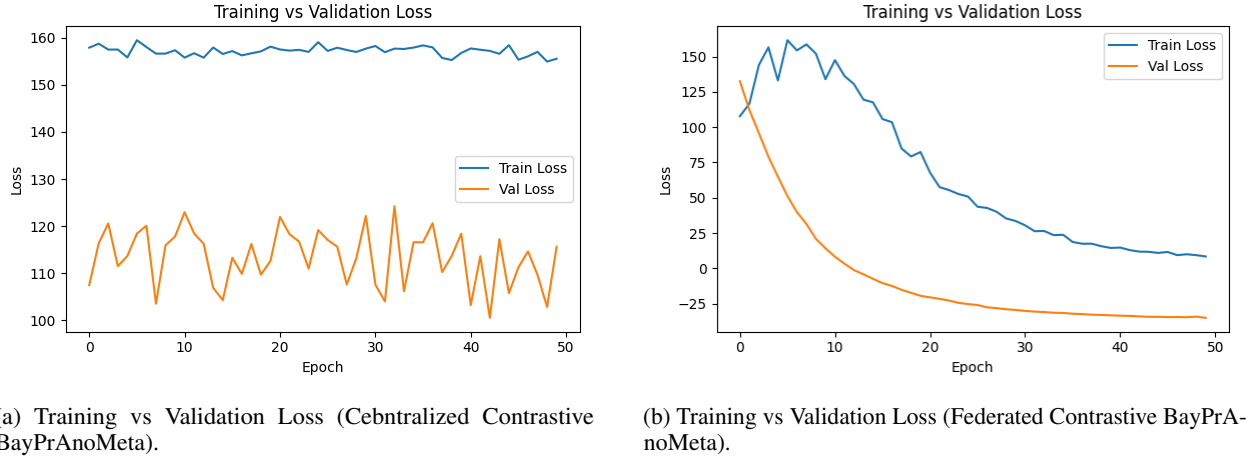


Figure 3: Comparison of training and validation loss curves of Federated BayPrAnoMeta (Bayesian Proto-MAML) and Federated Contrastive BayPrAnoMeta (Bayesian Proto-MAML).

The loss curves in Figure 3 further emphasize the role of contrastive learning in the federated setting. As shown in 3a, training and validation losses decrease steadily, reflecting client-specific distribution shifts and limited inter-client feature alignment. In contrast, 3b exhibits a more consistent and smoother decline in both training and validation loss, which validates improved optimization stability. The supervised contrastive loss acts as a cross-client regularizer, which aligns normal representations across clients despite non-i.i.d. data and episodic sampling. Thus, Figure 3 provides strong evidence supporting the inclusion of contrastive learning in the Federated BayPrAnoMeta framework, even when the performances are not uniform.



(a) Training vs Validation Loss (Centralized Contrastive BayPrAnoMeta).

(b) Training vs Validation Loss (Federated Contrastive BayPrAnoMeta).

Figure 4: Comparison of training and validation loss curves of Centralized Contrastive BayPrAnoMeta (Bayesian Proto-MAML) and Federated Contrastive Supervised BayPrAnoMeta (Bayesian Proto-MAML).

Figure 4 illustrates the distinct behaviors of centralized and federated BayPrAnoMeta frameworks through their loss curves. The centralized Contrastive BayPrAnoMeta framework shows a nearly flat training loss and a highly unstable validation loss, suggesting ineffective optimization and poor generalization. Conversely, the Federated Contrastive BayPrAnoMeta pipeline exhibits a steadily decreasing training loss and a rapidly converging validation loss, which is indicative of stable meta-optimization and enhanced generalization across tasks.

## G More Experimental Results

Table 4: PatchCore AUROC (%) across MVTec AD object categories under different training data fractions.

Category	PatchCore-1	PatchCore-10	PatchCore-50	PatchCore-100
Bottle	$100.0 \pm 0.00$	$100.0 \pm 0.00$	$100.0 \pm 0.00$	$100.0 \pm 0.00$
Cable	$45.0 \pm 0.81$	$49.2 \pm 0.77$	$48.2 \pm 0.84$	$49.8 \pm 0.81$
Capsule	$71.8 \pm 0.56$	$71.4 \pm 0.57$	$67.8 \pm 0.57$	$68.2 \pm 0.57$
Carpet	$50.0 \pm 0.62$	$47.4 \pm 0.64$	$49.0 \pm 0.64$	$46.7 \pm 0.63$
Grid	$40.0 \pm 0.80$	$42.6 \pm 0.81$	$45.5 \pm 0.80$	$42.4 \pm 0.83$
Hazelnut	$45.2 \pm 0.55$	$43.3 \pm 0.59$	$46.0 \pm 0.59$	$47.2 \pm 0.62$
Leather	$44.4 \pm 0.69$	$37.9 \pm 0.69$	$37.9 \pm 0.69$	$38.0 \pm 0.69$
Metal_nut	$47.8 \pm 0.60$	$52.4 \pm 0.63$	$50.0 \pm 0.65$	$49.0 \pm 0.65$
Pill	$43.8 \pm 0.59$	$41.3 \pm 0.53$	$46.5 \pm 0.55$	$46.9 \pm 0.56$
Screw	$66.6 \pm 0.45$	$56.0 \pm 0.56$	$52.9 \pm 0.57$	$50.0 \pm 0.53$
Tile	$51.5 \pm 0.63$	$50.5 \pm 0.64$	$52.8 \pm 0.62$	$51.6 \pm 0.61$
Transistor	$61.5 \pm 0.85$	$63.2 \pm 0.95$	$67.5 \pm 0.88$	$68.1 \pm 0.86$
Wood	$58.4 \pm 0.82$	$56.6 \pm 0.85$	$55.2 \pm 0.90$	$55.9 \pm 0.90$
Zipper	$71.2 \pm 0.53$	$62.5 \pm 0.64$	$65.8 \pm 0.62$	$66.8 \pm 0.61$

Table 5: PatchCore AUPRC (%) across MVTec AD object categories under different training data fractions.

Category	PatchCore-1	PatchCore-10	PatchCore-50	PatchCore-100
Bottle	100.0 $\pm$ 0.00	100.0 $\pm$ 0.00	100.0 $\pm$ 0.00	100.0 $\pm$ 0.00
Cable	26.4 $\pm$ 0.70	27.2 $\pm$ 0.71	29.6 $\pm$ 0.79	27.5 $\pm$ 0.70
Capsule	72.0 $\pm$ 0.68	73.1 $\pm$ 0.70	68.6 $\pm$ 0.72	69.0 $\pm$ 0.72
Carpet	48.4 $\pm$ 0.69	47.9 $\pm$ 0.69	46.8 $\pm$ 0.68	43.3 $\pm$ 0.64
Grid	47.5 $\pm$ 0.78	50.4 $\pm$ 0.80	52.7 $\pm$ 0.80	51.9 $\pm$ 0.81
Hazelnut	35.2 $\pm$ 0.65	33.9 $\pm$ 0.67	33.1 $\pm$ 0.65	34.6 $\pm$ 0.68
Leather	39.6 $\pm$ 0.69	39.9 $\pm$ 0.70	40.2 $\pm$ 0.72	40.3 $\pm$ 0.72
Metal_nut	55.0 $\pm$ 0.72	60.2 $\pm$ 0.77	58.9 $\pm$ 0.76	57.5 $\pm$ 0.75
Pill	50.0 $\pm$ 0.65	48.5 $\pm$ 0.62	50.7 $\pm$ 0.59	50.8 $\pm$ 0.60
Screw	60.1 $\pm$ 0.59	54.0 $\pm$ 0.64	51.7 $\pm$ 0.65	41.5 $\pm$ 0.61
Tile	48.9 $\pm$ 0.75	45.8 $\pm$ 0.75	42.5 $\pm$ 0.73	41.3 $\pm$ 0.70
Transistor	35.5 $\pm$ 1.05	39.2 $\pm$ 1.09	45.0 $\pm$ 1.15	43.9 $\pm$ 1.13
Wood	54.6 $\pm$ 0.96	55.2 $\pm$ 0.98	56.4 $\pm$ 0.98	57.3 $\pm$ 0.98
Zipper	67.2 $\pm$ 0.67	62.4 $\pm$ 0.75	65.9 $\pm$ 0.74	66.5 $\pm$ 0.74

Table 6: PatchCore F1 score (%, optimal threshold) across MVTec AD object categories under different training data fractions.

Category	PatchCore-1	PatchCore-10	PatchCore-50	PatchCore-100
Bottle	100.0 $\pm$ 0.00	100.0 $\pm$ 0.00	100.0 $\pm$ 0.00	100.0 $\pm$ 0.00
Cable	37.2 $\pm$ 0.65	37.3 $\pm$ 0.61	39.0 $\pm$ 0.70	38.4 $\pm$ 0.66
Capsule	75.1 $\pm$ 0.46	73.9 $\pm$ 0.47	73.8 $\pm$ 0.47	73.9 $\pm$ 0.47
Carpet	59.8 $\pm$ 0.49	58.4 $\pm$ 0.46	58.6 $\pm$ 0.46	58.6 $\pm$ 0.48
Grid	56.2 $\pm$ 0.57	57.6 $\pm$ 0.55	58.6 $\pm$ 0.55	57.3 $\pm$ 0.56
Hazelnut	51.8 $\pm$ 0.53	47.6 $\pm$ 0.53	48.5 $\pm$ 0.54	48.6 $\pm$ 0.54
Leather	55.4 $\pm$ 0.55	54.4 $\pm$ 0.53	54.6 $\pm$ 0.54	54.9 $\pm$ 0.54
Metal_nut	69.2 $\pm$ 0.47	68.4 $\pm$ 0.50	68.5 $\pm$ 0.49	68.6 $\pm$ 0.49
Pill	66.8 $\pm$ 0.44	67.0 $\pm$ 0.44	66.6 $\pm$ 0.42	66.9 $\pm$ 0.41
Screw	62.1 $\pm$ 0.44	57.1 $\pm$ 0.42	56.0 $\pm$ 0.43	55.3 $\pm$ 0.43
Tile	55.8 $\pm$ 0.52	54.7 $\pm$ 0.51	56.5 $\pm$ 0.54	56.5 $\pm$ 0.53
Transistor	44.1 $\pm$ 0.92	51.4 $\pm$ 0.98	57.0 $\pm$ 1.02	57.0 $\pm$ 1.02
Wood	61.3 $\pm$ 0.74	59.2 $\pm$ 0.70	59.3 $\pm$ 0.68	60.2 $\pm$ 0.69
Zipper	64.7 $\pm$ 0.50	60.4 $\pm$ 0.55	62.3 $\pm$ 0.56	62.8 $\pm$ 0.57

Table 7: AUPRC (%) across MVTec AD object categories for several baselines.

Category	PatchCore-25	Classical MAML	Classical Proto-MAML	BayPrAnoMeta	Better Performance?
Bottle	<b>100.0 <math>\pm</math> 0.00</b>	27.1 $\pm$ 0.64	95.3 $\pm$ 0.35	96.1 $\pm$ 0.33	$\times$
Cable	28.3 $\pm$ 0.74	41.9 $\pm$ 0.79	90.8 $\pm$ 0.59	<b>93.3 <math>\pm</math> 0.48</b>	$\checkmark$
Capsule	<b>71.0 <math>\pm</math> 0.69</b>	39.7 $\pm$ 0.79	48.8 $\pm$ 0.96	51.4 $\pm$ 0.98	$\times$
Carpet	46.8 $\pm$ 0.68	71.8 $\pm$ 0.95	84.5 $\pm$ 0.76	<b>90.6 <math>\pm</math> 0.60</b>	$\checkmark$
Grid	<b>50.3 <math>\pm</math> 0.79</b>	41.3 $\pm$ 0.73	37.5 $\pm$ 0.72	44.4 $\pm$ 0.85	$\times$
Hazelnut	31.9 $\pm$ 0.63	53.3 $\pm$ 0.97	47.4 $\pm$ 0.89	<b>55.9 <math>\pm</math> 1.00</b>	$\checkmark$
Leather	37.6 $\pm$ 0.68	46.5 $\pm$ 1.06	78.6 $\pm$ 0.83	<b>82.9 <math>\pm</math> 0.77</b>	$\checkmark$
Metal_nut	64.1 $\pm$ 0.71	34.3 $\pm$ 0.81	74.2 $\pm$ 1.07	<b>74.5 <math>\pm</math> 1.07</b>	$\checkmark$
Pill	49.2 $\pm$ 0.61	<b>52.5 <math>\pm</math> 1.10</b>	44.4 $\pm$ 0.85	48.3 $\pm$ 0.91	$\times$
Screw	<b>51.2 <math>\pm</math> 0.67</b>	32.8 $\pm$ 0.65	35.7 $\pm$ 0.76	38.8 $\pm$ 0.71	$\times$
Tile	42.2 $\pm$ 0.71	93.3 $\pm$ 0.49	96.4 $\pm$ 0.30	<b>98.9 <math>\pm</math> 0.16</b>	$\checkmark$
Transistor	40.6 $\pm$ 1.08	53.5 $\pm$ 1.05	66.4 $\pm$ 0.95	<b>70.2 <math>\pm</math> 0.92</b>	$\checkmark$
Wood	55.8 $\pm$ 0.98	53.5 $\pm$ 0.91	98.3 $\pm$ 0.18	<b>99.1 <math>\pm</math> 0.12</b>	$\checkmark$
Zipper	65.6 $\pm$ 0.74	51.1 $\pm$ 0.99	89.0 $\pm$ 0.63	<b>90.3 <math>\pm</math> 0.58</b>	$\checkmark$

Table 8: F1 score (%, optimal threshold) across MVTec AD object categories for several baselines.

Category	PatchCore-25	Classical MAML	Classical Proto-MAML	BayPrAnoMeta	Better Performance?
Bottle	<b>100.0 ± 0.00</b>	41.4 ± 0.23	93.1 ± 0.40	94.3 ± 0.38	✗
Cable	38.4 ± 0.65	52.4 ± 0.49	88.5 ± 0.58	<b>91.1 ± 0.52</b>	✓
Capsule	<b>73.0 ± 0.47</b>	50.9 ± 0.59	56.0 ± 0.61	59.5 ± 0.57	✗
Carpet	58.4 ± 0.46	71.2 ± 0.90	82.7 ± 0.71	<b>88.9 ± 0.63</b>	✓
Grid	57.9 ± 0.56	55.7 ± 0.44	53.5 ± 0.52	<b>60.4 ± 0.60</b>	✓
Hazelnut	48.4 ± 0.55	57.7 ± 0.75	59.7 ± 0.64	<b>65.8 ± 0.68</b>	✓
Leather	54.5 ± 0.53	51.6 ± 0.79	76.8 ± 0.76	<b>80.8 ± 0.73</b>	✓
Metal_nut	68.6 ± 0.49	44.9 ± 0.42	75.9 ± 0.80	<b>76.0 ± 0.81</b>	✓
Pill	<b>66.8 ± 0.43</b>	57.6 ± 0.84	55.5 ± 0.58	57.8 ± 0.59	✗
Screw	<b>56.4 ± 0.42</b>	47.5 ± 0.36	49.6 ± 0.49	53.0 ± 0.43	✗
Tile	55.9 ± 0.53	91.5 ± 0.56	94.5 ± 0.39	<b>97.9 ± 0.28</b>	✓
Transistor	53.7 ± 1.01	59.9 ± 0.80	70.8 ± 0.67	<b>74.3 ± 0.64</b>	✓
Wood	59.0 ± 0.68	59.9 ± 0.69	96.9 ± 0.32	<b>98.2 ± 0.25</b>	✓
Zipper	62.2 ± 0.56	55.4 ± 0.68	86.7 ± 0.64	<b>88.0 ± 0.58</b>	✓

Table 9: AUPRC (%) comparison across MVTec AD object categories for ablation studies.

Category	Contrastive BayPrAnoMeta	Federated BayPrAnoMeta	Federated Contrastive BayPrAnoMeta
Bottle	50.6 ± 1.64	86.2 ± 0.78	<b>86.8 ± 0.79</b>
Cable	<b>89.1 ± 0.65</b>	43.4 ± 0.99	42.4 ± 1.01
Capsule	43.7 ± 0.96	<b>58.9 ± 1.07</b>	53.9 ± 1.09
Carpet	<b>43.0 ± 1.12</b>	37.2 ± 1.11	42.3 ± 1.16
Grid	44.9 ± 0.87	<b>45.2 ± 0.93</b>	43.3 ± 0.88
Hazelnut	60.9 ± 1.08	70.8 ± 1.08	<b>72.1 ± 1.05</b>
Leather	39.4 ± 1.31	44.8 ± 1.08	<b>48.7 ± 1.13</b>
Metal_nut	<b>63.4 ± 1.18</b>	55.1 ± 1.05	57.6 ± 0.99
Pill	41.5 ± 0.96	<b>43.5 ± 0.94</b>	37.2 ± 0.80
Screw	38.3 ± 0.77	<b>51.2 ± 1.18</b>	36.1 ± 0.93
Tile	35.9 ± 1.23	<b>42.5 ± 0.97</b>	39.3 ± 0.93
Transistor	<b>54.7 ± 1.02</b>	30.8 ± 0.71	32.2 ± 0.80
Wood	57.3 ± 1.35	59.8 ± 1.65	<b>67.5 ± 1.55</b>
Zipper	62.1 ± 1.30	66.4 ± 1.24	<b>79.5 ± 1.07</b>

Table 10: F1 score (%, optimal threshold) comparison across MVTec AD object categories for ablation studies.

Category	Contrastive BayPrAnoMeta	Federated BayPrAnoMeta	Federated Contrastive BayPrAnoMeta
Bottle	58.2 ± 1.19	85.1 ± 0.77	<b>85.8 ± 0.78</b>
Cable	<b>86.9 ± 0.66</b>	55.8 ± 0.71	55.8 ± 0.73
Capsule	52.6 ± 0.64	<b>63.2 ± 0.80</b>	59.7 ± 0.81
Carpet	52.6 ± 0.74	50.0 ± 0.74	<b>53.0 ± 0.79</b>
Grid	<b>59.3 ± 0.64</b>	54.9 ± 0.61	54.3 ± 0.58
Hazelnut	66.2 ± 0.75	72.6 ± 0.84	<b>74.1 ± 0.83</b>
Leather	52.8 ± 0.87	54.4 ± 0.74	<b>56.6 ± 0.79</b>
Metal_nut	<b>67.8 ± 0.84</b>	62.3 ± 0.71	63.2 ± 0.68
Pill	53.5 ± 0.65	<b>54.6 ± 0.68</b>	50.9 ± 0.55
Screw	51.4 ± 0.47	<b>58.3 ± 0.80</b>	48.7 ± 0.57
Tile	49.3 ± 0.81	<b>54.1 ± 0.67</b>	51.9 ± 0.62
Transistor	<b>61.1 ± 0.73</b>	47.1 ± 0.49	47.5 ± 0.50
Wood	61.7 ± 1.00	66.5 ± 1.14	<b>71.6 ± 1.13</b>
Zipper	65.9 ± 0.98	68.3 ± 0.97	<b>78.9 ± 0.93</b>

## H Error Analysis

We analyze the learned embedding spaces using two-dimensional t-SNE projections of query embeddings to better understand the behavior of different models beyond performance metrics reported in section 5. These visualizations

would provide qualitative insights into class separability, representation collapse, and failure modes in few-shot anomaly detection.

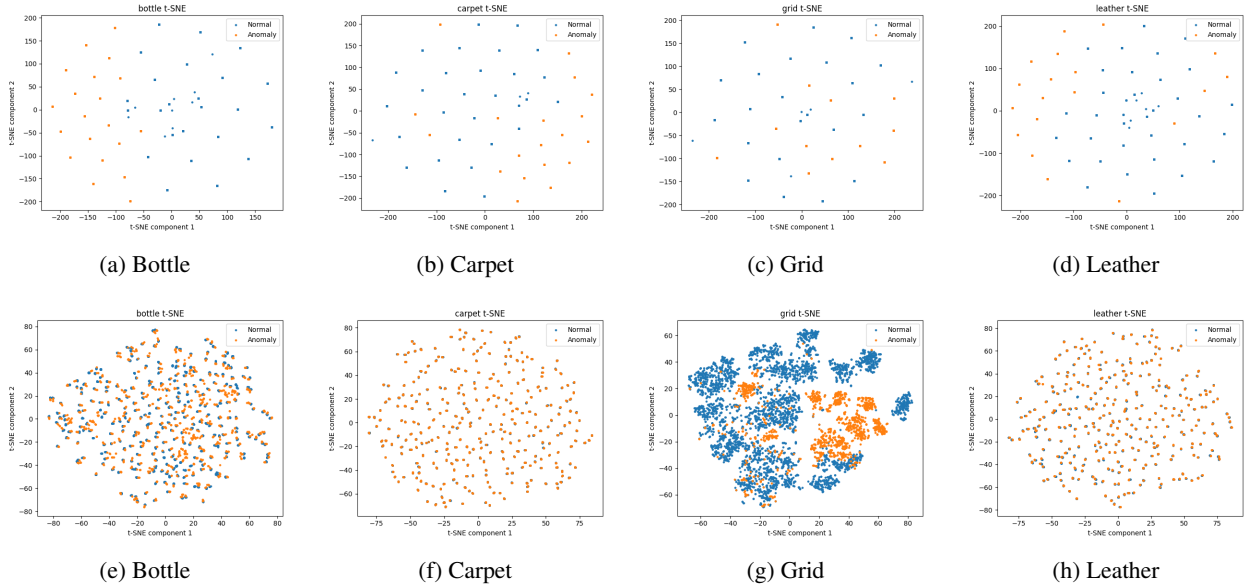


Figure 5: t-SNE visualizations. Upper (a) - (d): BayPrAnoMeta (Centralized). Lower (e) - (h): Contrastive BayPrAnoMeta (Centralized).

For Contrastive BayPrAnoMeta (Centralized), Figure 5 reveals that t-SNE embeddings show evidence of contrastive collapse, where normal and anomalous query embeddings cluster too tightly or align along a low-variance manifold. This collapse is particularly evident in object categories such as *Bottle*, *Carpet*, *Grid*, and *Leather*; where contrastive learning aggressively enforces intra-class compactness based on limited support samples.

Under our data preparation protocol, the contrastive objective is trained with incomplete class information, since the support set contains only normal samples. Consequently, the contrastive loss can unintentionally pull normal and unseen anomaly embeddings closer together in the feature space, which can reduce class separability. This effect explains the observed drop in anomaly detection performance. This explains why Contrastive BayPrAnoMeta (Centralized) can underperform its non-contrastive counterpart despite stronger representation regularization.

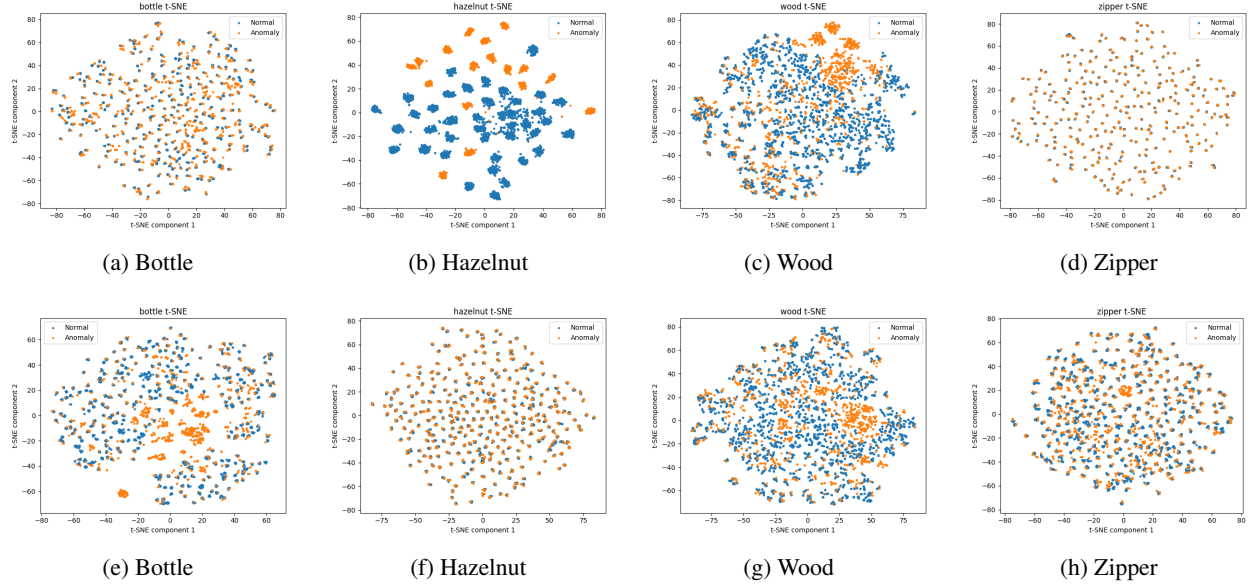


Figure 6: t-SNE visualizations. Upper (a) - (d): Contrastive BayPrAnoMeta (Centralized). Lower (e) - (h): Federated Contrastive BayPrAnoMeta.

The t-SNE visualizations of Figure 6 provide direct insight into the failure modes observed in Table 2. In the Contrastive BayPrAnoMeta (Centralized) setting, the t-SNE plots consistently show strong embedding collapse, where query normal samples and query anomalies overlap heavily in the latent space. In several object categories (e.g., *Bottle*, *Wood*, *Zipper*), anomaly embeddings are tightly clustered within or adjacent to normal clusters. This geometric overlap explains the near-random AUROC (Table 2) and degraded AUPRC (Table 9).

In contrast, in the Federated Contrastive BayPrAnoMeta t-SNE embeddings exhibit greater inter-class dispersion and reduced collapse across most objects. While perfect separation is still not achieved, anomaly embeddings tend to form looser, partially separated regions away from the dominant normal manifold. This structural improvement is consistent with the gains reported in Table 2, particularly for clients *Bottle*, *Hazelnut*, *Wood*, and *Zipper*. The federated setting exposes the global model to heterogeneous normality distributions across clients to regularize contrastive objective, which prevents excessive contraction of the embedding space.

Overall, the t-SNE analysis (Figure 5 and Figure 6) confirms that contrastive learning is not flawed, but highly sensitive to supervision completeness and data heterogeneity. While centralized contrastive learning amplifies embedding collapse under weak anomaly semantics, federated learning takes care of this issue by diversifying the learned representation space, which justifies the inclusion of contrastive loss in the Federated BayPrAnoMeta framework despite its weaker centralized performance.

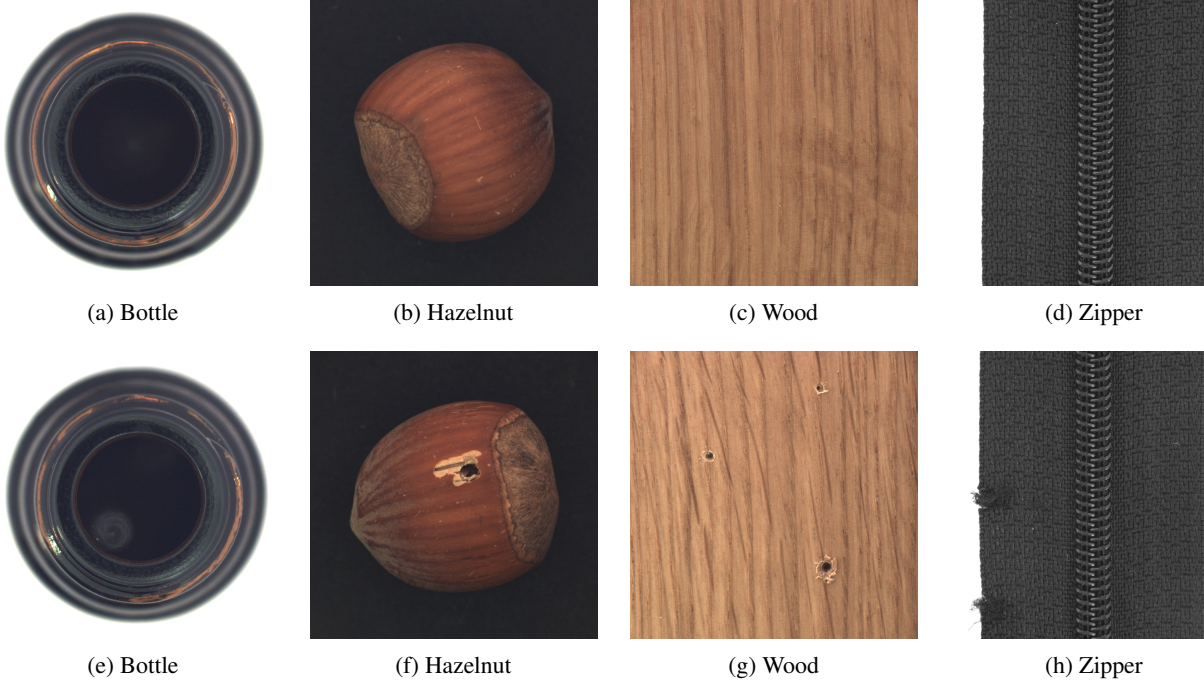


Figure 7: Misclassified Images of Federated Contrastive BayPrAnoMeta. Upper (a) - (d): False Positive images of clients *Bottle*, *Hazelnut*, *Wood*, *Zipper*. Lower (e) - (h): False Negative images of clients *Bottle*, *Hazelnut*, *Wood*, *Zipper*.

Figure 7 shows some images that are misclassified. or the clients *Bottle*, *Hazelnut*, *Wood*, and *Zipper*, and these errors are consistent with the contrastive embedding behavior observed in the corresponding t-SNE visualizations (Figure 6). For clients *Bottle* and *Hazelnut*, false positives predominantly occur in visually normal samples that exhibit specular highlights, subtle surface texture variations, or mild color inconsistencies.

In our proposed framework, we characterize normal embeddings by task specific Normal-Inverse-Wishart (NIW) distribution and heavy tailed distribution like Student- $t$  distribution is used for anomaly detection. Localized intensity variations in such images cause the support embeddings to scatter more widely. This reduces the likelihood of visually valid normal samples under the normal model,  $p_0(z | S_\tau)$ , but these samples still receive a non-negligible likelihood under the fixed, heavy-tailed anomaly reference distribution,  $p_1(z)$ . This imbalance directly inflates the anomaly score,  $s(x) = \log p_1(z) - \log p_0(z | S_\tau)$ , leading to an increased rate of false positives. Conversely, false negatives for *Bottle* and *Hazelnut* arise when defects such as small dents, internal contaminations, or minor surface irregularities induce only weak deviations from the learned normal embedding distribution, resulting in insufficient contrast against the anomaly model.

For client *Wood*, errors are primarily driven by its highly heterogeneous texture. False positives occur when strong grain variations or illumination changes increase intra-class embedding dispersion, which mainly causes normal samples to fall outside the high-density region of the learned normal manifold. At the same time, genuine anomalies such as fine cracks or knots often preserve the overall texture statistics, leading to false negatives because these samples remain well explained by the posterior predictive distribution. In the case of client *Zipper*, false positives are commonly associated with specular reflections or slight misalignments of the metallic teeth, which perturb embeddings without corresponding to true defects. False negatives typically correspond to subtle, shape-preserving defects such as minor tooth deformations or stitching inconsistencies. Due to partial embedding collapse, these anomalies retain a high likelihood under  $p_0(z | S_\tau)$ , resulting in missed detections.